Utilization of O_4 slant column density to derive aerosol layer height from a spaceborne UV-Visible hyperspectral sensor: Sensitivity and case study

Sang Seo Park[1], Jhoon Kim[1,*], Hanlim Lee[1,2], Omar Torres[3], Kwang-Mog Lee[4], Sang Deok Lee[5]

[1]Department of Atmospheric Science, Yonsei University, Seoul, Korea.

[2]Department of Spatial Information Engineering, Pukyong National University, Busan, Korea

[3]NASA Goddard Space Flight Center, Greenbelt, Maryland, United States

[4]Department of Astronomy and Atmospheric Science, Kyungpook National University, Daegu, Korea

[5]National Institute of Environment Research, Ministry of Environment, Incheon, Korea

* Correspondence to: Jhoon Kim (jkim2@yonsei.ac.kr)

Tel. : +82-2-2123-5682, Fax: +82-2-365-5163

Abstract

The sensitivities of oxygen-dimer (O_4) slant column densities (SCDs) to changes in aerosol layer height are investigated using the simulated radiances by a radiative transfer model, the Linearlized pseudo-spherical vector discrete ordinate radiative transfer (VLIDORT), and the Differential Optical Absorption Spectroscopy (DOAS) technique. The sensitivities of the O4 index (O4I), which is defined as dividing O_4 SCD by 10^{40} molecules^{2}cm^{-5}, to aerosol types and optical properties are also evaluated and compared. Among the O_4 absorption bands at 340, 360, 380, and 477 nm, the O_4 absorption band at 477 nm is found to be the most suitable to retrieve the aerosol effective height. However, the O4I at 477 nm is significantly influenced not only by the aerosol layer effective height but also by aerosol vertical profiles, optical properties including single scattering albedo (SSA), aerosol optical depth (AOD), particle size, and surface albedo. Overall, the error of the retrieved aerosol effective height is estimated to be 1276, 846, and 739 m for dust, non-absorbing, and absorbing aerosol, respectively, assuming knowledge on the aerosol vertical distribution shape. Using radiance data from the Ozone Monitoring Instrument (OMI), a new algorithm is developed to derive the aerosol effective height over East Asia after the determination of the aerosol type and AOD from the MODerate resolution Imaging Spectroradiometer (MODIS). About 80% of retrieved aerosol effective heights are within the error range of 1 km compared to those obtained from the Cloud-Aerosol Lidar with Orthogonal Polarization (CALIOP) measurements on thick aerosol layer cases.

1. Introduction

Aerosol is one of the key atmospheric constituents in understanding climate changes with its effects on direct and diffuse solar radiation (e.g., Haywood and Shine, 1995; Kaufman *et al.*, 2002), and plays an important role in air quality near the surface (e.g., Watson *et al.*, 1994; Prospero, 1999). For these reasons, observations from satellite remote sensing have been carried out to investigate aerosol properties at regional and global scale, including aerosol optical depth (AOD) (e.g., Curier *et al.*, 2008; Levy *et al.*, 2007; Torres *et al.,* 2007; Ahn *et al.*, 2014; Veefkind *et al.*, 1999; Zhang *et al.*, 2011), fine mode fraction (FMF) or Angstrom Exponent (AE) (e.g., Jones and Christopher, 2007; Lee *et al.*, 2010; Nakajima and Higurashi, 1998; Remer *et al.*, 2008), single scattering albedo (SSA) (e.g., Dubovik *et al.*, 2002; Levy *et al.*, 2007; Jeong and Hsu, 2008; Torres *et al.*, 1998, 2005, 2007; Jethva *et al.*, 2014), and aerosol types (e.g., Higurashi and Nakajima, 2002; Kim *et al.*, 2007; Lee *et al.*, 2010). These information were further utilized to estimate radiative forcing of aerosol (e.g., Christopher *et al.*, 2006; Chung *et al.*, 2005; Chou *et al.*, 2002), to understand the mechanism of the changes to the cloud formation (Twomey *et al.,* 1984; Albrecht, 1989; Jones *et al.,* 1994), and to monitor air quality (e.g., Wang and Christopher, 2003; Hutchison *et al.,* 2005).

Vertical profiles of atmospheric aerosols are affected by processes of formation, transport and deposition, and vary for different aerosol types over East Asia (Shimizu *et al.*, 2004). Labonne *et al.* (2007) also reported that the layer top height of biomass burning aerosol ranged from 1.5 to 7 km in the wild fire regions. The information on the aerosol layer height is important, because the variation of the aerosol vertical distribution affects radiative process in the atmosphere near the surface and trace gas

retrieval for air mass factor calculation. Uncertainty in aerosol layer height also affects the accuracy of AOD and SSA retrieval algorithms that use near UV observations (Torres *et al.*, 1998; Torres *et al.*, 2007; Jethva *et al.*, 2014) and complicates the interpretation of the Aerosol Index (AI), a qualitative parameter commonly used to detect absorbing aerosols (Herman *et al.*, 1997; Torres *et al.,* 1998). In addition, there have been difficulties to estimate surface concentration of aerosol from AODs, because the information on aerosol vertical distribution is not readily available and even hard to predict from the state-of-the-art models due to its large variability. Although the Cloud-Aerosol Lidar with Orthogonal Polarization (CALIOP) has been successful and provided vertical profiles of aerosols, its spatial coverage was very limited with its measurement characteristics (Omar *et al.*, 2009). Liu *et al.* (2005) showed that the Particulate Matter (PM) concentration estimated by the AOD from satellite observation accounted for only 48% of the measured surface PM, although their study reflected variations of the aerosol types and its hygroscopic growth in the algorithms. One of the essential factors to consider in estimating PM from AOD is the vertical structure of aerosols (e.g. Chu, 2006; Seo *et al.*, 2015). Therefore, conventional aerosol products would benefit significantly with the development of robust algorithm to retrieve aerosol height using satellite data.

The Differential Optical Absorption Spectroscopy (DOAS) technique has been used widely to retrieve trace gas concentration both from ground-based (e.g., Platt, 1994; Platt and Stutz, 2008) and space-borne (e.g., Wagner et al., 2007; Wagner *et al.*, 2010) measurements. After the work of Platt (1994) to retrieve trace gas concentration by using DOAS, Wagner et al. (2004) suggested to derive atmospheric aerosol information from O_4 measurement by using Multi Axis Differential Optical Absorption

90 Spectroscopy (MAX-DOAS). Friess et al. (2006) analyzed the model studies to
91 calculate the achievable precision of the aerosol optical depth and vertical profile. In
92 addition, several studies (e.g., Irie *et al.*, 2009 and 2011; Lee *et al.*, 2009 and 2011;
93 Clemer *et al.*, 2010; Li *et al.*, 2010) provided aerosol profiles from ground-based
94 hyperspectral measurements in UV and visible wavelength ranges on several ground
95 sites. Wagner *et al.* (2010) investigated the sensitivity of various factors to the aerosol
96 layer height using the data obtained from the SCanning Imaging Absorption
97 SpectroMeter for Atmospheric ChartographY (SCIAMACHY) on ENVISAT. The
98 sensitivity of the Ring effect and the absorption by oxygen molecule (O_2) and its dimer
99 (O_4) calculated by DOAS method were examined to estimate aerosol properties
100 including the layer height. Kokhanovsky and Rozanov (2010) estimated dust altitudes
101 using the O_2-A band between 760 and 765 nm after the determination of the dust
102 optical depth. In addition, several previous studies are also investigated estimation
103 methods for aerosol height information by using hyperspectral measurement in visible
104 (e.g., Dubuisson *et al.*, 2009; Koppers and Murtagh, 1997; Sanders and de Haan, 2013;
105 Sanghavi *et al.*, 2012; Wang *et al.*, 2012). Because the surface signal is significantly
106 smaller than the aerosol signal in the near UV, these wavelength regions are useful to
107 derive aerosol height information from space borne measurements.

108 For OMI measurement, the O_4 band at 477 nm has been widely applied to
109 estimate cloud information (e.g., Accarreta *et al.*, 2004; Sneep *et al.*, 2008). Especially,
110 the cloud information retrieved by O_4 band at 477 nm was used to analyze air mass
111 factor (AMF) with the consideration of aerosol optical effects for the NO_2 column
112 retrieval (e.g., Castellanos et al., 2015, Chimot et al., 2015; Lin et al., 2014; Lin et al.,
113 2015). Although O_4 absorption band around 477 nm varies also due to cloud existence,

it can be also used for the aerosol optical parameter estimation. Veihelmann *et al.* (2007) introduced that the 477 nm channel, a major O_4 band, significantly adds degree of freedom for aerosol retrieval by using principal component analysis, and Dirksen *et al.* (2009) adopts the pressure information obtained from OMI O_4 band to identify a plume height for aerosol transport cases.

In this study, the sensitivities of the O_4 bands at 340, 360, 380, and 477 nm to changes in aerosol layer height and its optical properties are estimated using simulated hyperspectral radiances, differently from the previous studies using the O_2-A band observation (e.g., Kokhanovsky and Rozanov, 2010). We proposed an improved DOAS algorithm for the O_4 absorption bands to retrieve aerosol height information from the O_4 slant column densities (SCDs) based on the sensitivity studies. This new algorithm is applied to the O_4 SCD from the Ozone Monitoring Instrument (OMI) to retrieve the aerosol effective height (AEH) for a real case over East Asia, including error estimates.

2. Methods

In general, scattering by aerosol at low altitudes leads to an increase in the length of the average light path (enhancement effect), while those at high altitudes causes a decrease in the length of the average light path (shielding effect) (Wagner *et al.*, 2010). These two opposing effects change the estimated O_4 SCD values. Furthermore, the measured O_4 SCD is a function of wavelength, because the absorption and scattering by atmospheric molecules and aerosols have spectral dependence. Therefore, radiative transfer calculations are carried out to estimate the sensitivity of the O_4 SCD with respect to the change of atmospheric conditions. Details of the radiative transfer model

(RTM) and input parameters to simulate radiance are discussed in section 2.1. Analytical method of the DOAS to estimate the O_4 is described in section 2.2.

2.1. Simulation of hyperspectral radiance

Figure 1 shows the flowchart of the method to estimate the O_4 SCD from the simulated radiance. Because the magnitude of the O_4 SCD values is too large to express the sensitivity results, this paper defines the O_4 index (O4I) which divides O_4 SCD by 10^{40} molecules^{2}cm^{-5}. In order to investigate the sensitivities of the O4I at several bands in UV and visible wavelengths with respect to various aerosol properties, including AEHs, aerosol amounts and aerosol types, the hyperspectral radiance is simulated using the Linearlized pseudo-spherical vector discrete ordinate radiative transfer (VLIDORT) model (Spurr, 2006). The VLIDORT model is based on the linearized discrete ordinate radiative transfer model (LIDORT) (Spurr et al., 2001; Spurr, 2002). This RTM is suitable for the off-nadir satellite viewing geometry of passive sensors since this model adopts the spherically curved atmosphere to reflect the pseudo-spherical direct-beam attenuation effect (Spurr *et al.*, 2001). The model calculates the monochromatic radiance ranging from 300 to 500 nm with a spectral resolution of 0.1 nm. The radiance spectrum is calculated with a 0.2 nm sampling resolution applying a slit response function (SRF) given by a normalized Gaussian distribution with 0.6 nm as the full-width half maximum (FWHM).

2.1.1. Aerosol properties

The aerosol input parameters for the RTM are important in simulating the radiance spectra because aerosol optical properties determine scattering and absorption

characteristics. The data from the Optical Properties of Aerosol and Cloud (OPAC) package (Hess *et al.*, 1998) are used as aerosol parameters, which includes the spectral complex refractive indices and size distribution of aerosols, to calculate SSA and phase function through the Mie calculations. The information of the aerosol parameters is not available at the UV wavelengths, since the AERONET observation provides the information of those aerosol parameters in the visible.

In terms of the aerosol types, water soluble (WASO), mineral dust (MITR), and continental polluted (COPO) model are selected to simulate non-absorbing aerosol, mineral dust, and absorbing anthropogenic aerosol, respectively. The COPO is combined type including both soot and WASO, which represents the pure black-carbon and non-absorbing aerosols, respectively. The mixture of these two types, adequately describes the fine mode aerosol from anthropogenic pollution. The SSA is the largest for WASO and the smallest for COPO. In order to account for hygroscopic growth, the default relative humidity is assumed to be 80 % (c.f., Holzer-Popp and Schroedter-Homscheidt, 2004).

2.1.2. Aerosol vertical distribution

In this present study, 'aerosol height' refers to aerosol effective height (AEH), defined as the peak height in Gaussian distribution. According to Hayasaka *et al.* (2007), however, the aerosol extinction coefficient was found to exponentially decrease with altitude over East Asia based on the ground-based LIDAR observation data during the Atmospheric Brown Clouds-East Asia Regional Experiment 2005 (ABC-EAREX 2005) campaign. Previous studies used the exponentially decreasing pattern with altitude to represent the aerosol vertical profiles (e.g. Hayasaka *et al.*,

2007; Li *et al.*, 2010), and reported that aerosol is present within 5 km in altitude for most of the cases (e.g. Sasano, 1996; Chiang *et al.*, 2007). On the other hands, the aerosol vertical distribution does not always follow exponential profile. For the long-range transported aerosol such as dust cases, the aerosol layer profile is quite different than exponential profile and occasionally transported to well above the boundary layer (e.g., Reid et al., 2002; Johnson et al., 2008). The peak height of aerosol extinction profile in long-range transport cases was reported to be located between 1 and 3 km during the Dust and Biomass-burning Aerosol Experiment (DABEX) campaign (Johnson et al., 2008). From these previous studies, standard aerosol vertical profile is difficult to determine. For algorithm development, previous studies assumed that the vertical distribution is Gaussian function defined by peak height and half width as representative parameters (Torres et al., 1998; Torres et al., 2005). To supplement the simplicity of assumption for aerosol vertical distribution, aerosol vertical distributions are assumed to be quasi-Gaussian generalized distribution function (GDF), which is Gaussian distribution with dependence on aerosol peak height, width, and layer top and bottom height. Details of GDF can be found in Spurr and Christi (2014) and Yang et al. (2010). In this study, AEH ranges from 1 to 5 km with 1 km width as 1-sigma for the RTM simulation.

2.1.3. Atmospheric gases

The vertical distribution of the O_4 number density, which is used to calculate its SCD from the RTM, is assumed to be the square of the O_2 number density in each layer (Hermans *et al.*, 2003). Thus, the total number of the O_4 column density from surface to TOA is 1.38×10^{43} molecule^{2}cm^{-5}, where 93% and 73% of the total O_4 is

distributed below the altitude of 10 km and 5 km, respectively. In particular, signals by the changes of O_4 are strong below 5 km, where aerosol transports are observed frequently. The vertical distributions of other atmospheric components are taken from the US standard atmosphere 1976 (United States Committee on Extension to the Standard Atmosphere, 1976). The vertical distribution of trace gases and aerosol in the troposphere are interpolated in the 0.1 km resolution from the sea level to 5 km.

2.2. DOAS analysis for O4I estimation

Table 1 summarizes the absorption cross sections of trace gases used as inputs for the radiance simulations and the DOAS spectral analysis. At wavelengths of 340, 360, 380, and 477 nm, the O_4 absorption cross section from Hermans *et al.* (1999) is used in this study. O_3 absorption cross sections at three different temperatures (223, 243, and 273 K) and NO_2 absorption cross sections at two different temperatures (220 and 294 K) are used to account for the amounts in the stratosphere and the troposphere. The radiance information obtained from the RTM simulation is analyzed to derive the O_4 SCDs using WinDOAS software (van Roozendael and Fayt, 2001) before O4I estimation. To analyze the simulated radiances, the spectrum calculated without all atmospheric gases and aerosol are used as the Fraunhofer reference spectrum (FRS). The simulated spectra are fitted simultaneously with the absorption cross sections of all trace gases listed in Table 1 and FRS in the respective wavelength range of 335-350, 350-370, 370-390, and 460-486 nm, using a nonlinear least squares method (Platt and Stutz, 2008).

On the other hand, the O4I from OMI standard product of cloud (OMCLDO2) (e.g., Accarreta et al., 2004; Sneep et al., 2008) is used to adopt the AEH retrieval for

234 case study. The OMCLDO2 basically used the cross section database from Newnham
235 and Ballard (1998) considering the temperature dependence by interpolating to
236 representative atmospheric temperature of 253 K (Accarreta et al., 2004). For this
237 reason, there can be systematic difference between the O4I from OMCLDO2 and
238 direct estimation from the observed radiance spectra in this present study. Figure 2
239 shows the O_4 SCD from OMCLDO2 and those directly retrieved from radiance
240 spectrum over all observed OMI pixels on March 31, 2007 over East Asia. Similar to
241 the DOAS analysis using the simulated spectra for a look-up table (LUT) calculation,
242 OMI observed radiance spectra are fitted with the Ring spectrum and the FRS in
243 addition to the absorption cross sections in Table 1 within the same wavelength
244 window. Before the spectral fitting, the NO_2 and O_3 cross sections are I_0 corrected, and
245 the Ring spectrum (Fish and Jones, 1995), accounting for the effects of the rotational
246 Raman scattering due to air molecules, is calculated using the WinDOAS software
247 (van Roozendael and Fayt, 2001). After the fitting, the noise level of residual spectrum
248 is estimated to be on the order of 10^{-3} for the radiance spectrum at 477 nm from OMI
249 measurements. The O_4 SCDs with the fitting error less than 1% is used for the
250 comparison. From this figure, a systematic difference between the two different fitting
251 results is less than 1%, although the cross section databases for fitting are different.
252 From this result, the effect of cross section database difference is negligible when the
253 same observation data was used. Furthermore, the DOAS analysis for LUT calculation
254 can be used to compare the O_4 SCD from OMCLDO2.
255 Figure 3 shows the comparison of the O_4 SCD at 477 nm from LUT with the
256 dimension as in Table 2 against OMCLDO2 for aerosol and cloud free pixels in year
257 2005. The LUT of O_4 SCD is estimated by the DOAS analysis using simulated

radiance from VLIDORT with various geometries as shown in Table 2. The clear sky region is selected for the Pacific Ocean with cloud fraction less than 0.02 from OMI observation. The surface albedo is assumed to be 0.05, which is similar to the minimum Lambertian equivalent reflectance (LER) over clear ocean surface (e.g., Kleipool et al., 2008). Because the standard product of the O_4 SCD is only estimated at the 477 nm band, the results can be compared only at this band. To minimize the DOAS fitting error, the observed data from OMI is selected by the fitting precision less than 2% and the quality flags for spectral fitting are also considered. As shown in Figure 3(a), the coefficient of determination (R^2) is 0.864 with a slope of 1.050, and the LUT exhibits a ratio of 0.86±0.05 to the values obtained from OMI standard values. Despite the statistically significant R^2 and slope values between the two values, there exists negative bias by about 14%.

The bias between the retrieved from LUT and the estimated from standard product values can be attributed to the differences in the O_4 cross section data and the lack of their temperature and pressure dependence as noted from the previous works by Wagner *et al.* (2009), Clemer *et al.* (2010), and Irie et al. (2015). For this reason, ground-based measurements adopted the correction factors to cross section database. However the bias effect for the cross section difference is limited as shown in Figure 2, and the correction factor for the cross section database in the previous studies cannot be adopted to the space-borne measurements. From Kleipool et al. (2008), the minimum LER is defined to be the 1% cumulative probability threshold, and frequent LER value are typically higher than minimum LER over clear ocean, although cloud screening was perfectly executed before LER calculation. To account for the difference between simulated and observed SCD, the LUT was re-calculated by

changing condition to the surface albedo of 0.10. Although assumed surface albedo is higher than minimum LER from Kleipool et al. (2008), the surface albedo of 0.10 is realistic value for ocean surface albedo at mid-latitude (e.g., Payne, 1972). The corrected result is shown in Figure 3(b), with the R^2 of 0.865 similar to that before the correction, while the negative bias is removed to 0.98±0.05 and the regression line slope is 1.123. Although the comparison result is not perfect, the calculation by the VLIDORT simulates the satellite observation and can be used for sensitivity tests and case studies to retrieve aerosol height.

3. Sensitivity test

3.1. Sensitivity of the O4Is to the AEH

The sensitivity of the O4I to the AEH is investigated for its absorption bands at 340, 360, 380, and 477 nm. Figure 4 shows the O4I as a function of the AEH and the three different aerosol types of MITR, WASO and COPO at 360, 380, and 477 nm, respectively. The vertical error bar represents the fitting error estimated by the residual spectra from the DOAS fitting (e.g., Stutz and Platt, 1996). For the calculation shown in the figures, the following geometries are assumed: solar zenith angle (SZA) of 30 degrees, viewing zenith angle (VZA) of 30 degrees, and relative azimuth angle (RAA) of 100 degrees. Note that insignificant SCD value was estimated at 340 nm due to the large spectra fitting error. In these three figures, the O4Is show the AEHs ranging from 1.0 to 5.0 km for the AODs of 1.0 and 2.5 at 500 nm, which could be due to the existence of thick aerosol layers. For the sensitivity result, the decrease rate of the O4I value in the 1 km interval of AEH ($-dO_4/dZ$) is defined as equivalent O4I difference converting from O4I difference between neighbor AEH in same AOD condition.

306 The O4Is are estimated at 360 and 380 nm band as shown in Figure 4(a) ~ (f).
307 The O4I is significantly decreased with increasing AEH at 360 and 380 nm for all
308 aerosol types. However negative O4Is are occasionally estimated at 360 nm.
309 Furthermore the fitting errors are too large to estimate the AEH, which range from 160
310 to 410 at 360 nm and from 350 to 1060 at 380 nm. From large fitting error with small
311 O4I, the fitting results are insignificant at these two absorption bands.

312 On the other hand, the sensitivity of the O4I at 477 nm is a significant variable to
313 estimate AEH. The mean value of $-dO_4/dZ$ is estimated to be 87, 290, and 190 for the
314 MITR, WASO, and COPO when the AOD is 1.0, respectively. The mean value of -
315 dO_4/dZ on the AOD of 2.5 is estimated to be 94, 362, and 213 for the MITR, WASO,
316 and COPO, respectively. The calculated $-dO_4/dZ$ are significantly larger than the mean
317 O4I fitting errors of 58, which implies that the O4I at 477 nm is useful in estimating
318 the AEH. The small fitting errors at 477 nm are due to the larger O_4 absorption and
319 less interferences by other trace gases in this spectral window.

320 Figure 5 shows $-dO_4/dZ$ as changing viewing geometries. As enlarging
321 geometrical path length for viewing geometry, $-dO_4/dZ$ also increases because the path
322 length through the aerosol layer is also increased. The mean value of $-dO_4/dZ$
323 including all cases of AEH is estimated to be 90 to 326 at SZA of 30.0 degree and
324 VZA of 30.0 degree, while it is estimated to be 265 to 485 at SZA of 60.0 degree and
325 VZA of 60.0 degree. Although aerosol scattering angle is changed by SZA and VZA,
326 the O4I sensitivity to AEH is generally increased to increasing optical path length to
327 the viewing geometries. From this result, the accuracy for the AEH retrieval is
328 potentially better for large zenith angle cases than for low zenith angle cases.
329

330 ### 3.2. Error analysis

331 Errors are also estimated in terms of key variables in the estimation of the O4I at
332 477 nm, with the variables and their dimensions as summarized in Table 3. For the
333 error analysis of AEH retrieval, characteristics for all of extinction properties are
334 essential to consider. In this study, errors are analyzed in terms of AOD, aerosol
335 vertical distribution, particle size and SSA for aerosol amount and properties. Surface
336 albedo variation is also considered to represent surface condition. To estimate the error
337 amount, the AEH error is converted from the half of O4I difference between adding
338 and deducting perturbation of variables as shown in equation (1).

339 $$\varepsilon(Z) = \left| \frac{O4I(x+\delta x,Z) - O4I(x-\delta x,Z)}{2.0 \times dO4I/dZ(x,Z)} \right| \quad (1)$$

340 where $\varepsilon(Z)$ is the AEH error amount due to variable of error source, x, in AEH
341 of Z, and δx is perturbation of AEH retrieval error source. The $\varepsilon(Z)$ value also
342 depends on viewing geometries. Therefore $\varepsilon(Z)$ is represented for specific geometries
343 together with averaging over all geometries.

344

345 #### 3.2.1. AOD

346 The O4I at 477 nm has sensitivity not only for AEH but for AOD as shown in
347 Figure 4(g) ~ (i). Because the radiance extinction by aerosol changes depending on
348 AOD, the optical path length of TOA radiance is also affected by AOD. For different
349 AODs (τ_a), the O4I at AEHs of 1.0 and 3.0 km is shown in Figure 6 for the same
350 geometry assumed in Figure 4. From OMI standard products, the expected error of the
351 AOD over ocean is the larger of 0.1 or 30% for absorbing aerosol, and the larger of 0.1
352 or 20% for non-absorbing aerosol (Torres et al., 1998, 2002). For this reason, the

353 uncertainty of AOD is assumed to be 0.1 in this study, although uncertainty of AOD
354 would be larger than the assumed value for large AOD. The decreasing rate of the O4I
355 ($-dO_4/d\tau_a$), which defines O4I reduction with AOD increase by 0.1, is found to be
356 larger for the AEH at 3.0 km than for that at 1.0 km. Among the three aerosol types,
357 the $-dO_4/d\tau_a$ is found to be the least for the WASO, which has stronger scattering
358 characteristics than other two aerosol types. In addition, the sensitivity for WASO
359 showed negative $-dO_4/d\tau_a$ for small AOD at low AEH, which has small shielding
360 effect with large enhancement effect, due to the large SSA of WASO. The mean -
361 $dO_4/d\tau_a$ values are estimated to be 1.2%, 0.9%, and -0.1% for the AEH of 1.0 km as
362 the AOD changes by 0.1 for the MITR, COPO, and WASO, respectively, whereas
363 they are estimated to be 2.3%, 2.1%, and 1.0% for the AEH of 3.0 km with respect to
364 the same AOD changes for the three different type, respectively.

365 Figure 7 shows the expected error in AEH due to retrieval uncertainty of AOD
366 from observation. Because O_4 concentration exponentially decreases as the
367 atmospheric altitude increases, the sensitivity to AEH becomes weak at high AEHs. In
368 addition, aerosol signal is relatively weak for low AOD. From these reasons, the AEH
369 retrieval error due to AOD uncertainty is maximized for the high AEH with low AOD
370 cases for all aerosol types. The maximum retrieval error is 2.0, 0.7, and 4.4 km for
371 COPO, WASO, and MITR for the case at AEH of 4.0 km and AOD of 0.4, which is
372 least sensitive case for AEH. For AOD of 0.4, however, the retrieval error due to AOD
373 uncertainty is 0.3, 0.2, and 0.4 km for COPO, WASO, and MITR for the case at AEH
374 of 1.0 km. Except for AEH lower than 4 km and AOD larger than 0.4, the retrieval
375 error of AEH is less than 1.0 km for all viewing geometries and all aerosol types.

376 Furthermore, the AEH error for AOD uncertainty is also dependent on viewing

377 geometries. From previous studies, the error for cloud height information depends on
378 the observation geometries due to changing average optical path length (Accarreta et
379 al., 2004; Chimot et al., 2015). Moreover, the retrieval error sensitivity for observation
380 geometries is also found in aerosol height estimation by O_2-A band (Sanders et al.,
381 2015). Similar to these previous studies, the AEH error becomes larger for short light
382 paths and smaller for long paths. Figure 8 shows the viewing geometry dependence of
383 AEH error for AOD of 1.0. With the increase in effective optical path length, the
384 radiance signal from aerosol is also enhanced. In general, the AEH error decreases
385 with increasing viewing geometries. For WASO case, however, the AEH error is
386 smaller for short path length than long path length in low AEH case. For thin aerosol
387 layer situation, the radiance is enhanced by scattering aerosols which results in
388 increasing optical path length. In the small SZA and VZA, aerosol layer effectively
389 brings enhancement effect. With increasing SZA and VZA, however, the shielding
390 effect due to aerosol layer enhances because radiance has to pass through long path
391 through aerosol layer. For this reason, the smallest error case is inflection point of
392 AOD sensitivity, which corresponds to turnaround point between with larger shielding
393 effect than enhancement effect.
394
395 **3.2.2. SSA**
396 Torres *et al.* (1998) showed that the result of the SSA from OMI can be
397 overestimated due to the cloud contamination, although aerosol retrieval algorithm
398 considers the existence of cloud in sub-pixel. Furthermore, the SSA varies widely for
399 different aerosol types. Therefore, the sensitivity of O4I to the SSA variation is
400 estimated for the same geometries used in the previous tests. To estimate O4I

401 sensitivity to the SSA variation, the imaginary part of refractive index value
402 corresponding to 10% variability for SSA is changed after fixing the real part of
403 refractive index. The mean O4I changes by 106, 282, and 205 for MITR, WASO, and
404 COPO, respectively, with respect to its SSA deviation by 10%. To compare the
405 difference for WASO and COPO, it is proportional to the absolute values of the SSA
406 for all simulated cases. In addition, the difference for MITR is smaller than those for
407 COPO, because less fraction of back scattering in coarse mode particle makes less
408 sensitive to O4I.

409 Figure 9 shows the AEH error due to the SSA variation by 10%. Because of the
410 low sensitivity characteristics of AEH as shown in section 3.1, thus large errors are
411 shown for high AEH and low AOD cases. However, the AEH errors are less than 1 km
412 for COPO aerosol type. For AOD of 1.0, the AEH error due to SSA variation is
413 estimated to be 610 to 900 m for the COPO type. Furthermore, the error is calculated
414 to range from 270 to 1220 m and from 930 to 1400 m for COPO and WASO type,
415 respectively, if AEH is 3 km, frequently assumed reference altitude in aerosol retrieval
416 algorithm (e.g., Torres et al., 1998). For MITR, dust-like type aerosol, AEH error,
417 which ranges from 410 to 1430 m for AOD of 1.0, is generally the largest compared to
418 those of other aerosol types. In general, uncertainty of aerosol optical properties is
419 large for thin aerosol layer case, thus that of the AEH is as well.

420

421 **3.2.3. Particle size**

422 Aerosol particle size has noticeable effects on the phase function, thus the
423 directional scattered intensity. However, most of aerosol retrieval algorithm assumes
424 aerosol particle size depending on its type as an input parameter to RTM calculation.

425 Although aerosol type is categorized, however, physical properties of aerosol can be
426 changed according to the source type and transport characteristics. In the OMI aerosol
427 algorithm, size distribution is one of error sources for the AOD (Torres et al., 2002).

428 Figure 10 shows the AEH error due to particle size change. For error estimation,
429 mode radius difference for number size distribution is assumed to be ±20%, which
430 corresponds to larger range by 4 times than those from the error budget study for OMI
431 standard product (Torres et al., 2002). Overall, O4I difference is within the order of
432 100. The coarse mode aerosol, MITR in this study, results in the largest O4I difference
433 for all cases, thus the largest AEH error for MITR which is estimated to range from
434 0.2 to 2.7 km. On the other hand, the error ranges from 0.03 to 0.5 km and from 0.2 to
435 1.9 km for WASO and COPO, respectively. The largest AEH errors for the three
436 aerosol types are estimated for the case with AOD of 0.4 and AEH at 5.0 km.

437

438 **3.2.4. Surface Albedo**

439 As the surface albedo affects the $-dO_4/dZ$, the sensitivity of the O4I is also tested
440 with respect to the surface albedo difference of 0.02. The difference of climatological
441 surface albedo between that obtained from the total ozone monitoring spectrometer
442 (TOMS) and the global ozone monitoring experiment (GOME) was known to be up to
443 0.02 (Koelemeijer *et al.*, 2003). Table 4 shows the sensitivity of the O4I with respect to
444 the change in the surface albedo. The absolute difference of O4I due to surface albedo
445 variation is below 85. Because aerosol layer attenuates the reflected radiance from
446 surface, the absolute difference of O4I value decreases as aerosol amount increase.
447 Furthermore, it is found that the difference of O4I due to surface albedo change is
448 larger for the non-absorbing aerosol than the absorbing aerosol, because absorbing

aerosol attenuates the reflected radiance more than the non-absorbing aerosol. In terms of AEH change, the O4I difference increases as AEH increase. For low AEH case, optical path length of reflected radiance from surface to aerosol layer is relatively short as compared to high AEH case. For this reason, the O4I sensitivity for surface albedo is reduced by high concentration of aerosol near the surface for the low AEH case.

Figure 11 shows the expected retrieval error of AEH due to surface albedo difference as changing AEH with respect to AOD and its types. As mentioned in previous section, the $-dO_4/dZ$ is small in high AEH and low AOD cases. Furthermore, the albedo sensitivity increases as AEH increases and AOD decreases. As a result, the AEH error is frequently larger than 1 km for high AEH with small AOD, especially when AOD is less than 0.4. Because reflected radiance from surface is dominant for thin aerosol case, the AEH error in high AEH with low AOD shows the largest value as compared to previous error analysis. However, the AEH error sharply decreases as AOD increases and AEH decreases, when aerosol signal becomes dominant. Especially for MITR, four simulation cases, when AOD = 0.4 with AEH > 3.0 km and AOD = 1.0 with AEH = 5.0 km, show the AEH error larger than 1 km. Because $-dO_4/dZ$ is too small in these cases, AEH retrievals in the four simulation cases show limitation as a reliable result. For COPO and WASO, however, all the cases in AEH < 3.0 km, which directly influence surface concentration, show error lower than 750 m even for the assumed AOD of 0.4. In addition, errors less than 500 m are found for AOD > 1.0 with AEH < 3.0 km.

3.2.5. Vertical distribution

Aerosol vertical distribution varies largely by distance from source, atmospheric

dynamics during aerosol transport, and sink mechanism in reality. To estimate the AEH error due to variation of aerosol vertical distribution, the half-width of GDF distribution was doubled for comparison. Although it is not possible here to consider all kinds of aerosol vertical distributions due to its large variability in profile, aerosol vertical distribution by changing the half-width of GDF distribution can reflect large-scale changes in its vertical profile.

Table 5 shows the mean AEH errors between the two vertical profiles of aerosol as AOD changes. As the aerosol vertical profile is changed with increasing its widths, the difference of O4I ranges from 100 to 430. Because aerosol vertical profile simultaneously affects aerosol concentration and layer thickness, the O4I difference shows large value as the vertical distribution changes. For this reason, the AEH error is larger than 2.5 km for all aerosol types with AOD of 0.4. The estimated errors caused solely by the change between the two aerosol vertical profiles, range 1477±602, 722±190, and 671±265 m for the MITR, COPO, and WASO, respectively, for AOD greater than 1.0.

3.3. Error budget

Table 6 shows the summary of the total error budget for the AEH estimation with a list of the major error sources and their values, assuming errors in each variable in OMI standard products. To convert the O4I difference to the AEH error, the difference of O4I due to the respective error source is divided by that from the change of the AEH in each bin of the AOD and AEH as shown in section 3.2, with the simulation cases over 58,800 runs listed in Table 3 to calculate mean and standard deviation of errors. Because of weak signal sensitivity to AEH for AOD of 0.4 and AEH at 5.0 km as

497 shown in the previous section, this simulation case is omitted in calculating statistical
498 values for error budget. In summary, the total number of aerosol simulations for the
499 combination of AOD and AEH includes 39 cases.

500 The mean errors from 10% variation in the SSA for all of the variable conditions
501 in Table 3 correspond to 726, 576, and 1047 m for the MITR, COPO, and WASO,
502 respectively. For the total error budget calculations, however, SSA change by 5% was
503 used according to Torres *et al.* (2007), which reported the variation of the SSA less
504 than 0.03 for the given aerosol type. The error from the vertical distribution is
505 estimated to be 720, 1480, and 690 m for the COPO, MITR and WASO, respectively.

506 The errors from SSA and aerosol profile shape are the two important error
507 sources in estimating the AEH, followed by the errors related to AOD and surface
508 albedo. From these results, the errors of the AEH due to the error from OMI AOD of
509 0.1 and the surface albedo of 0.02 are less than 300 m for WASO and COPO, and
510 about 400 m for MITR. However, the AEH error from surface albedo is important for
511 cases with low AOD at high AEH, which is surface reflectance dominant case.

512 The mean errors from 20% variation in the aerosol particle size are 726, 576, and
513 1047 m for the MITR, COPO, and WASO, respectively. Torres et al. (2002) assumed
514 the variation of size distribution to be 5%. Thus, for the total error budget calculations
515 assuming 5% change in the particle size, the AEH errors are less than 100 m. In
516 addition, the errors in the O4I, and thereby the AEH, are associated with the variations
517 in the column amounts and the differences in the absorption cross section of each fitted
518 trace gas for the spectral analysis. The variations in the column amounts of trace gases
519 and the differences in the absorption cross section values do not affect significantly in
520 calculating the O4I. However, the O_4 vertical column density is changed by the change

in atmospheric pressure. In East Asia, the surface pressure over ocean is 1010.9±29.6 (3-sigma) hPa from NCEP Reanalysis 2 data since 2004. In clear case, the difference of O4I due to the ±3% for pressure variation is 3.4±0.1% in all geometries.

Furthermore, the AEH error in terms of inaccurate spectral wavelength calibration is estimated based on the assumed errors of ±0.02 nm, which corresponds to 0.1 pixels for OMI. Although it is well known that the accuracy in the spectral wavelength calibration before the DOAS fitting affects the trace gas SCD retrieval, the errors in the O4I associated with the wavelength shift of the sub-pixel scale are estimated to be negligible due to the broad O_4 absorption band width around 477 nm.

Finally, the total error budget in the AEH retrieval is estimated based on the error analysis with respect to error sources. Note that the result of error analysis explains about 50% for SSA and 25% for size parameter in calculating the total error budget. Overall, the total error budget in the AEH retrieval is estimated to be 739, 1276, and 846 m for the COPO, MITR, and WASO, respectively, with the exception of the contribution of the errors in the aerosol vertical profiles. Therefore accurate assumption for optical properties of aerosol is essential to develop the retrieval algorithm of aerosol height.

4. Case study

To demonstrate the feasibility from real measurements, the AEHs are derived using hyperspectral data from OMI. OMI channels are composed of UV-1 (270-314 nm), UV-2 (306-380 nm), and a visible wavelength range (365-500 nm) with a spectral resolution (FWHM) of 0.63, 0.42, and 0.63 nm, respectively (Levelt *et al.*, 2006). The spatial resolution is 13 km × 24 km at nadir in "Global Mode". In the

present study, the OMI spectral data over the visible wavelength range are used to derive the O4I at 477 nm and the AEH information.

Figure 12 shows an AEH retrieval algorithm for the case study. In retrieving AEH, AOD is obtained from MODIS standard product (e.g., Levy et al., 2007). Although OMI aerosol product provides AOD at 500 nm, AOD from OMI was partially affected by aerosol height and suffered from cloud contamination due to its large footprint (Torres et al., 2002). For this reason, AOD from MODIS was allocated to the OMI pixels as a reference AOD for the AEH retrieval. For type selection, the AE from MODIS and AI from OMI is respectively used for the information of size and absorptivity, to classify aerosol type into four following the method from Kim et al. (2007) and Lee et al. (2007). After determining AOD and aerosol type, LUT, which is generated as functions of geometries (SZA, VZA, and RAA), aerosol types and AODs, is used to determine the AEH information by comparing simulated with the measured O4I value. The variables and their dimensions for the LUT calculations are listed in Table 7. Due to the limitation of the accuracy of aerosol type classification and those of AOD over land, this study estimates the AEH only over ocean surface. Although temporal and spatial variation of surface albedo influences the AEH result from error study, surface albedo is assumed to be a fixed value of 0.10, which is used in the sensitivity study. If the surface albedo is changed but known, the qualitative conclusion here is not affected. For case study, the LUT of O4I is developed by the aerosol model based on AERONET data over East Asia. Extensive AERONET dataset over East Asia are used to provide represent aerosol optical properties for the LUT calculation.

Figure 13 shows the results of the retrieved AEH during the Asian dust event on

March, 31, 2007. MODIS products of AOD and FMF on this date show that thick dust layer with the AOD up to 1.0 from China to the Yellow Sea [Figure 13(b)] and the FMF ranging from 0.2 to 0.4, indicating the dominance of coarse-mode particles [Figure 13(c)]. Using the basis of the current algorithm with the pre-determined AOD and type, the mean retrieved AEH is 2.3±1.3 km over 647 pixels in East Asia [Figure 13(d)]. The retrieved result is compared with the backscattering intensity from the CALIOP observation over the Yellow Sea as shown in Figure 13(e). From CALIOP observation, the aerosol layer height over Yellow Sea is located at around 1 km altitude for most of observed regions. Over the Yellow Sea domain in 35~40 ˚N and 120~130 ˚E, the AEH from OMI is 1.5±1.1 km over 166 pixels, which is within 1 km difference from the CALIOP. From the retrieved result, the retrieved AEH is successfully retrieved within expected error, and the current algorithm quantitatively estimates the AEH over East Asia.

Figure 14 is another case study of the retrieved AEH on February, 21, 2008. MODIS products of AOD and FMF on this date show thick anthropogenic aerosol transported with the AOD ranging from 0.6 to 1.0 [Figure 14(b)] and the FMF ranging from 0.8 to 1.0 [Figure 14(c)] all over the Yellow Sea. The mean retrieved AEH is 1.4±1.2 km over 1480 pixels in East Asia as shown in Figure 14(d). On this date, CALIOP passed over coastal line between China and Yellow Sea. The aerosol layer height ranged from 0.5 to 2.5 km during the overpass over East Asia as shown in Figure 14(e). The AEH from OMI is 0.6±0.4 km over 601 pixels in 30~40 ˚N and 120~125 ˚E. Contrary to large spatial variation of the AEH from CALIOP, the AEH from OMI shows spatially stable values on this date.

Figure 15 shows the scatter plot of AEH between CALIOP and OMI on the dates

593 in Table 8, which lists aerosol transport cases over East Asia with simultaneous
594 observations by OMI and CALIOP in 2007 and 2008. The AEH from CALIOP is
595 estimated by the data from vertical profile of aerosol extinction coefficient at 532 nm.
596 Because the O4I sensitivity for AEH is not large at AEH higher than 4 km, the
597 comparison test was limited to cases with AEH less than 4.5 km from OMI. For data
598 collocation, the latitude and longitude difference between two sensors are within 0.25
599 degree. Figure 15(a) shows the comparison of AEH from OMI and CALIOP with
600 MODIS AOD larger than 0.5. It is assumed that the reference expected error (EE) is 1
601 km (Fishman et al., 2012). Almost 60% of retrieved pixel shows the AEH result within
602 the EE. Because of large AEH error for low AOD, the accuracy of AEH result from
603 OMI is poor. Furthermore, this case study assumes constant surface albedo value over
604 ocean. However, ocean surface albedo is also changed by turbidity due to sediments
605 and ocean surface due to wind. For this reason, the AEH error is exaggerated for low
606 AOD cases. If lower of AOD for the comparison is set to be 1.0, the proportion of
607 pixel within EE improves up to 80% as shown in Figure 15(b). Furthermore, the
608 correlation of the AEH between the two sensors is improved with the regression line
609 slope of 0.62 and the correlation coefficient (R) of 0.65 for thick aerosol layer cases.
610 Therefore, the AEH algorithm from OMI provides the reasonable information about
611 the parameter of aerosol vertical distribution, if accurate aerosol model is provided for
612 the forward calculation.
613
614 **5. Summary & discussion**
615 The sensitivities of the O4I at 340, 360, 380, and 477 nm bands are investigated
616 with RTM calculations to derive the AEH using the space-borne hyperspectral data.

Among these O_4 absorption bands, the O4I at 477 nm is considered to be suitable for the AEH retrieval. In addition to the AEH, AOD, aerosol type, aerosol vertical profile, particle size, and surface albedo are also found to have effects on the O4I at 477 nm, while the spectral calibration and cross section of the atmospheric gases have negligible effects on the O4I. The major error source for the AEH retrieval is found to be the uncertainty in SSA, which leads to the AEH error ranging from 270 to 1400 m with the SSA perturbation by 10%. In addition, the profile shape is also a major error source for the AEH estimation. According to the error estimations, the total errors are 739, 1276 m, and 846 m for absorbing, dust, and non-absorbing aerosol, respectively, due to combined uncertainties of the variation from AOD, SSA, particle size, and surface albedo.

In addition to the sensitivity analysis, an algorithm for the AEH derivation is developed for the first time based on a LUT that consists of the O4I in terms of the AEH, AOD, aerosol types, surface albedo, and measurement geometries. After the determination of AOD and aerosol types from the MODIS, the AEH value is derived over East Asia by the current algorithm using OMI measurement data. Considering the accuracy of AOD and aerosol types, the result is shown over ocean surface. From several cases for the long-range transport of aerosol over East Asia, the derived AEH shows reasonable value as compared to aerosol layer height from CALIOP with the correlation coefficient of 0.62 for AOD larger than 1.0. In addition, 80% of estimated AEH from OMI showed error less than 1 km in AEH.

There are many works to be done to improve the newly introduced algorithm as it requires the products from MODIS to determine the AOD and aerosol types prior to the AEH retrieval. The vertical distribution and the optical properties of the aerosol

need to be quantified using the combination of observation database, such as MPLNET and AERONET. Furthermore, the spatial variation of the AOD, surface pressure and the contamination by the cloud in the sub-pixel scale need to be investigated as they are also thought to affect the retrieved results. If the surface reflectance can be characterized with sufficient accuracy, the retrieval of the AEH can be extended to over land. In addition, the O4I method in this study can be applied to the surface pressure estimation in clear regions.

Acknowledgements

This work was supported by the Eco Innovation Program of KEITI (ARQ201204015), Korea, and it was also supported by the Brain Korea plus program.

References

Accarreta, J. R., De Haan, J. F., and Stammes, P.: Cloud pressure retrieval using the O2-O2 absorption band at 477 nm, *J. Geophys. Res.*, *109*, D05204, doi:10.1029/2003JD003915, 2004

Ahn, C., Torres, O., and Jethva, H.: Assessment of OMI near-UV aerosol optical depth over land, *J. Geophys. Res., 119,* 2457-2473, doi:10.1002/2013JD020188, 2014.

Albrecht, B. A.: Aerosols, cloud microphysics, and fractional cloudiness, *Science, 245*, 1227-1230, 1989.

Bogumil, K., Orphal, J., Burrows, J. P., and Flaud, J. M.: Vibrational progressions in the visible and near-ultraviolet absorption spectrum of ozone, *Chem. Phys. Lett.*, *349*, 241-248, 2001.

Castellanos, P., Boersma, K. F., Torres, O., and De haan, J. F.: OMI tropospheric NO2 air mass factors over South America: effects of biomass burning aerosols, *Atmos. Meas. Tech. Discuss, 8*, 2683-2733, 2015.

Chiang, C. -W, Chen, W. -N., Liang, W. -A., Das, S. K., and Nee, J.-B.: Optical properties of tropospheric aerosols based on measurements of lidar, sun-photometer and visibility at Chung-Li (25˚N, 121˚E), *Atmos. Env., 41*, 4128-4137, 2007.

Chimot, J., Vlemmix, T., Veefkind, J. P., De Haan, J. F., and Levelt, P. F.: Impact of aerosols on the OMI tropospheric NO2 retrievals over industrialized regions: how accurate is the aerosol correction of cloud-free scenes via a simple cloud model?, *Atmos. Meas. Tech. Discuss, 8*, 8385-8437, 2015.

Chou, M. -D, Chan, P. -K., and Wang, M.: Aerosol radiative forcing derived from SeaWiFS-Retrieved aerosol optical properties, *J. Atmos. Sci., 59*, 748-757, 2002.

Christopher, S. A., Zhang, J., Kaufman, Y. J., and Remer, L. A.: Satellite-based assessment of top of atmosphere anthropogenic aerosol radiative forcing over

679 cloud-free oceans, *Geophys. Res. Lett*, *33*, L15816, doi:10.1029/2005GL025535,
680 2006.
681 Chu, D. A.: Analysis of the relationship between MODIS aerosol optical depth and
682 PM2.5 in the summertime US., *Optics & Photonics. International Society for*
683 *Optics and Photonics,* 2006.
684 Chung, E. C., Ramanathan, V., Kim, D., and Podgorny. I. A.: Global anthropogenic
685 aerosol direct forcing derived from satellite and ground-based observations, *J.*
686 *Geophys. Res., 110,* D24207, doi:10.1029/2005JD006356, 2005.
687 Clemer, K., Van Roozendael, M., Fayt, C., Hendrick, F., Hermans, C., Pinardi, G.,
688 Spurr, R., Wang, P., and De Maziere, M.: Multiple wavelength retrieval of
689 tropospheric aerosol opticalproperties from MAXDOAS measurements in Beijing,
690 *Atmos. Meas. Tech., 3*, 863-878, doi:10.5194/amt-3-863-2010, 2010.
691 Curier, R. L., Veefkind, J. P., Braak, R., Veihelmann, B., Torres, O., and de Leeuw, G.:
692 Retrieval of aerosol optical properties from OMI radiances using a
693 multiwavelength algorithm: Application to western Europe, *J. Geophys. Res., 113*,
694 D17S90, doi:10.1029/2007JD008738, 2008.
695 Dirksen, R. J., Boersma, K. F., de Laat, J., Stammes, P., van der Werf, G. R., Martin, M.
696 V., and Kelder, H. M., An aerosol boomerang: Rapid around-the-world transport of
697 smoke from the December 2006 Australian forest fires observed from space, *J.*
698 *Geophys. Res., 114*, D21201, doi:10.1029/2009JD012360, 2009.
699 Dubovik, O., Holben, B., Eck, T. F., Smirnov, A., Kaufman, Y. J., King, M. D., Tanre,
700 D., and Slutsker, I.: Variability of absorption and optical properties of key aerosol
701 types observed in worldwide locations, *J. Atmos. Sci., 59*, 590-608, 2002.
702 Dubuisson, P., Frouin, R., Dessaily, D., Duforet, L., Leon, J. –F., Voss, K., and Antoine,
703 D.: Estimating the altitude of aerosol plumes over the ocean from reflectance ratio
704 measurements in the O2 A-band, *Remote Sens. Environ.*, *113*, 1899-1911,
705 doi:10.1016/j.rse.2009.04.018, 2009.
706 Fish, D. J., and Jones, R. L.: Rotational Raman scattering and the ring effect in zenith-
707 sky spectra, *Geophys. Res. Lett., 22*, 811-814, 1995.
708 Fishman, J., Iraci, L. T., Al-Saadi, J., Chance, K., Chavez, F., Chin, M., Coble, P.,
709 Davis, C., DiGiacomo, P. M., Edwards, D., Eldering, A., Goes, J., Herman, J., Hu,
710 C., Jacob, D. J., Jordan, C., Kawa, S. R., Key, R., Liu, X., Lohrenz, S., Mannino,

711 A., Natraj, V., Neil, D., Neu, J., Newchurch, M., Pickering, K., Salisbury, J., Sosik,
712 H., Subramaniam, A., Tzortziou, M., Wang, J., and Wang, M.: The United States'
713 Next Generation of Atmospheric Composition and Coastal Ecosystem
714 Measurements: NASA's Geostationary Coastal and Air Pollution Events (GEO-
715 CAPE) Mission. *Bull. Amer. Meteor. Soc., 93*, 1547-1566, 2012.
716 Friess, U., Monk, P. S., Remedios, J. J., Rozanov, A., Sinreich, R., Wagner, T., and
717 Platt, U.: MAX-DOAS O4 measurements: A new technique to derive information
718 on atmospheric aerosols: 2. Modeling studies, *J. Geophys. Res., 111*, D14203,
719 doi:10.1029/2005JD006618, 2006.
720 Hayasaka, T., Satake, S., Shimizu, A., Sugimoto, N., Matsui, I., Aoki, K., and Muraji,
721 Y.: Vertical distribution and optical properties of aerosols observed over Japan
722 during the Atmospheric Brown Clouds-East Asia Regional Experiment 2005, *J.*
723 *Geophys. Res., 112*, D22S35, doi:10.1029/2006JD008086, 2007.
724 Haywood, J. M. and Shine, K. P.: The effect of anthropogenic sulfate and soot aerosol
725 on the clear sky planetary radiation budget, *Geophys. Res. Lett., 22*, 603-606, 1995.
726 Herman, J. R., Bhartia, P. K., Torres, O., Hsu, C., Seftor, C., and Celarier, E.: Global
727 distribution of UV-absorbing aerosols from Nimbus-7/TOMS data, *J. Geophys.*
728 *Res., 102*(D14), 16911-16922, 1997.
729 Hermans, C., Vandaele, A. C., Carleer, M., Fally, S., Colin, R., Jenouvrier, A., Coquart,
730 B., and Merienne, M.: Absorption Cross-sections of atmospheric constituents: NO2,
731 O2, and H2O, *Environ. Sci. Poll. Res., 6(3)*, 151-158, 1999.
732 Hermans, C., Vandaele, A. C., Fally, S., Carleer, M., Colin, R., Coquart, B., Jenouvrier,
733 A., and Merienne, M. F.: Absorption cross-section of the collision-induced bands
734 of oxygen from the UV to the NIR. In Weakly interacting molecular pairs:
735 unconventional absorbers of radiation in the atmosphere, (pp. 193-202), Springer
736 Netherlands, 2003.
737 Hess, M., Koepke, P., and Schult, I.: Optical properties of aerosols and clouds: The
738 software package OPAC, *B. Am. Meteorol. Soc., 79*(5), 831-844, 1998.
739 Higurashi, A., and Nakajima, T.: Detection of aerosol types over the East China Sea
740 near Japan from four-channel satellite data, *Geophys. Res. Lett, 29*(17), 1836,
741 doi:10.1029/2002GL015357, 2002.

742 Holzer-Popp, T., and Schroedter-Homscheidt, M.: Synergetic aerosol retrieval from
743 ENVISAT.In Proc. ERS/ENVISAT Symposium, Salzburg (Vol. 6, No. 10.9), 2004.
744 Hutchison, K. D., Smith, S., and Faruqui, S. J.: Correlating MODIS aerosol optical
745 thickness data with ground-based PM2.5 observations across Texas for use in a
746 real-time air quality prediction system, *Atmos. Env., 39*, 7190-7203, 2005.
747 Irie, H., Kanaya, Y., Akimoto, H., Iwabuchi, H., Shimizu, A., and Aoki, K.: Dual-
748 wavelength aerosol vertical profile measurements by MAX-DOAS at Tsukuba,
749 Japan, *Atmos. Chem. Phys., 9*, 2741-2749, 2009.
750 Irie, H., Takashima, H., Kanaya, Y., Boersma, K. F., Gast, L., Wittrock, F., Brunner, D.,
751 Zhou, Y., and Van Roozendael, M.: Eight-component retrievals from ground-based
752 MAX-DOAS observations, *Atmos. Meas. Tech., 4*, 1027-1044, 2011.
753 Irie, H., Nakayama, T., Shimizu, A., Yamazaki, A., Nagai, T., Uchiyama, A., Zaizen, Y.,
754 Kagamitani, S., and Matsumi, Y.: Evaluation of MAX-DOAS aerosol retrievals by
755 coincident observations using CRDS, lidar, and sky radiometer in Tsukuba, Japan,
756 *Atmos. Meas. Tech., 8*, 2775-2788, 2015.
757 Jeong, M., -J., and Hsu, N. C.: Retrievals of aerosol single-scattering albedo and
758 effective aerosol layer height for biomass-burning smoke: Synergy derived from
759 "A-Train" sensors, *Geophys. Res. Lett.*, Vol. 35, L24801,
760 doi:10.1029/2008GL036279, 2008.
761 Jethva, H., Torres, O., and Ahn, C.: Global assessment of OMI aerosol single-scattering
762 albedo using ground-based AERONET inversion, *J. Geophys. Res., 119*, 9020-
763 9040, doi:10.1002/2014JD021672, 2014.
764 Johnson, B. T., Heese, B., McFarlane, S. A., Chazette, P., Jones, A., and Bellouin, N.:
765 Vertical distribution and radiative effects of mineral dust and biomass burning
766 aerosol over West Africa during DABEX, *J. Geophys. Res.*, 113, D00C12,
767 doi:10.1029/2008JD009848, 2008.
768 Jones, A., Roberts, D. L., and Slingo, A.: A climate model study of indirect radiative
769 forcing by anthropogenic sulphate aerosols, *Nature, 370*, 450-453, 1994.
770 Jones, T. A., and Christopher, S. A.: MODIS derived fine mode fraction characteristics
771 of marine, dust, and anthropogenic aerosols over the ocean, constrained by
772 GOCART, MOPITT, and TOMS, *J. Geophys. Res., 112*, D22204,
773 doi:10.1029/2007JD008974, 2007.

774 Kaufman, Y. J., Tanre, D., and Boucher, O.: A satellite view of aerosols in the climate
775 system, *Nature, 419,* 215-223, 2002.
776 Kim, J., Lee, J., Lee, H. C., Higurashi, A., Takemura, T., and Song, C. H.: Consistency
777 of the aerosol type classification from satellite remote sensing during the
778 Atmospheric Brown Cloud – East Asia Regional Experiment campaign, *J.*
779 *Geophys. Res., 112*, D22S33, doi:10.1029/2006JD008201, 2007.
780 Kleipool, Q. L., Dobber, M. R., de Haan, J. F., and Levelt, P. F.: Earth surface
781 reflectance climatology from 3 years of OMI data, *J. Geophys. Res.*, 113,
782 D18308, doi:10.1029/2008JD010290, 2008.
783 Koelemeijer, R. B. A., de Haan, J. F., and Stammes, P.: A database of spectral surface
784 reflectivity in the range 335-772 nm derived from 5.5 years of GOME
785 observations, *J. Geophys. Res.,108*(D2), 4070, doi:10.1029/2002JD002429,
786 2003.
787 Kokhanovsky, A. A., and Rozanov, V. V.: The determination of dust cloud altitudes
788 from a satellite using hyperspectral measurements in the gaseous absorption band,
789 *Int. J. Rem. Sens., 31*, Nos. 9-10, 2729-2744, 2010.
790 Koppers, G. A. A., and Murtagh, D. P.: Retrieval of height resolved aerosol optical
791 thickness in the atmospheric band (Chapter 5), in G. A. A. Koppers, Radiative
792 transfer in the absorption bands of oxygen: Studies of their significance in ozone
793 chemistry and potential for aerosol remote sensing, Stockholm Univ., Stockholm,
794 Sweden, 1997.
795 Labonne, M., Breon, F. -M., and Chevallier, F.: Injection height of biomass burning
796 aerosols as seen from a spacebornelidar, *Geophys. Res. Lett., 34,* L11806,
797 doi:10.1029/2007GL029311, 2007.
798 Lee, H., Irie, H., Kim, Y. J., Noh, Y., Lee, C., Kim, Y., and Chun, K. J.: Retrieval of
799 aerosol extinction in the lower troposphere based on UV MAX-DOAS
800 measurements, *Aerosol Sci. Technol., 43(5),* 502-509, 2009.
801 Lee, H., Irie, H., Gu, M., Kim, J., and Hwang, J.: Remote sensing of tropospheric
802 aerosol using UV MAX-DOAS during hazy conditions in winter: Utilization of O4
803 absorption bands at wavelength intervals of 338-368 and 367-393 nm, Atmos. Env.,
804 doi:10.1016/j.atmosenv.2011.07.019, 2011.

Lee, J., Kim, J., Lee, H. C., and Takemura, T.: Classification of aerosol type from MODIS and OMI over East Asia, *Asia-Pacific J. Atmos. Sci., 43*, 4, 343-357, 2007.

Lee, J., Kim, J., Song, C. H., Ryu, J. -H., Ahn, Y. –H., and Song, C. K.: Algorithm for retrieval of aerosol optical properties over the ocean from the Geostationary Ocean Color Imager, *Remote Sens. Environ., 114*, 1077-1088, 2010.

Levelt, P. F., van den Oord, G. H. J., Dobber, M. R., Maelkki, A., Visser, H., de Vries, J., Stammes, P., Lundell, J. O. V., and Saari, H.: The Ozone Monitoring Instrument, *IEEE T. Geosci. Remote., 44*(5), 1093-1101, 2006.

Levy, R. C., Remer, L. A., Mattoo, S., Vermote, E. F., and Kaufman, Y. J.: Second-generation operational algorithm : Retrieval of aerosol properties over land from inversion of Moderate Resolution Imaging Spectroradiometer spectral reflectance, *J. Geophys. Res., 112*, D13211, doi:10.1029/2006JD007811, 2007.

Li, X., Brauers, T., Shao, M., Garland, R. M., Wagner, T., Deutschmann, T., and Wahner, A.: MAX-DOAS measurements in southern China: Retrieval of aerosol extinctions and validation using ground-based in-situ data, *Atmos. Chem. Phys., 10*, 2079-2089, 2010.

Lin, J. -T., Martin, R. V., Boersma, K. F., Sneep, M., Stammes, P., Spurr, R., Wang, P., Van Roozendael, M., Clemer, K., and Irie, H.: Retrieving tropospheric nitrogen dioxide from the Ozone Monitoring Instrument: effects of aerosols, surface reflectance anisotropy, and vertical profile of nitrogen dioxide, *Atmos. Chem. Phys., 14*, 1441-1461, 2014.

Lin, J. -T., Liu, M. -Y., Xin, J. -Y., Boersma, K. F., Spurr, R., Martin, R., and Zhang, Q.: Influence of aerosols and surface reflectance on satellite NO_2 retrieval: seasonal and spatial characteristics and implications for NOx emission constraints, *Atmos. Chem. Phys. Discuss., 15*, 12653-12714, 2015.

Liu, Y., Sarnat, J. A., Kilaru, V., Jacob, D. J., and Koutrakis, P.: Estimating ground-level PM2.5 in the Eastern United States using satellite remote sensing, *Environ. Sci. Technol., 39*, 3269-3278, 2005.

Nakajima, T., and Higurashi, A.: A use of two-channel radiances for and aerosol characterization from space, *Geophys. Res. Lett., 25(20)*, 3815-3818, 1998.

Newnham, D. A., and Ballard, J.: Visible absorption cross sections and integrated absorption intensities of molecular oxygen (O_2 and O_4), *J. Geophys. Res., 103*, No. D22, 28801-28816, 1998.

Omar, A. H., Winker, D. M., Kittaka, C., Vaughan, M. A., Liu, Z., Hu, Y., Trepte, C. R., Rogers, R. R., Ferrare, R. A., Lee, K. –P., Kuehn, R. E., and Hostetler, C. A.: The CALIPSO automated aerosol classification and lidar ratio selection algorithm, *J. Atmos. Oceanic Technol.*, Vol. 26, 1994-2014, 2009.

Payne, R. E.: Albedo of the Sea Surface, *J. Atmos. Sci.*, 29, 959-970, 1972.

Platt, U.: Differential optical absorption spectroscopy (DOAS), *Air monitoring by spectroscopic technique*, 127, 27-84, 1994.

Platt, U., and Stutz, J.: *Differential absorption spectroscopy*, Springer Berlin Heidelberg, 2008.

Prospero, J. M.: Long-term measurements of the transport of African mineral dust to the southeastern United States: Implications for regional air quality, *J. Geophys. Res., 104(D13)*, 15917-15927, 1999.

Reid, J. S., Westphal, D. L., Livingston, J. M., Savoie, D. L., Maring, H. B., Jonsson, H. H., Eleuterio, D. P., Kinney, J. E., Reid, E. A.: Dust vertical distribution in the Caribbean during the Puerto Rico Dust Experiment, *Geophys. Res. Lett., 29*, 7, 1151, doi:10.1029/2001GL014092, 2002.

Remer, L. A., Kleidman, R. G., Levy, R. C., Kaufman, Y. J., Tanre, D., Mattoo, S., Martins, J. V., Ichoku, C., Koren, I., Yu, H., and Holben, B. N.: Global aerosol climatology from the MODIS satellite sensors, *J. Geophys. Res., 113*, D14S07, doi:10.1029/2007JD009661, 2008.

Sanders, A. F. J. and de Haan, J. F.: Retrieval of aerosol parameters from the oxygen A band in the presence of chlorophyll fluorescence, *Atmos. Meas. Tech., 6*, 2725-2740, 2013.

Sanders, A. F. J., de Haan, J. F., Sneep, M., Apituley, A., Stammes, P., Vieitez, M. O., Tilstra, L. G., Tuinder, O. N. E., Koning, C. E., and Veefkind, J. P.: Evaluation of the operational Aerosol Layer Height retrieval algorithm for Sentinel-5 Precursor: application to O2 A band observations from GOME-2A, *Atmos. Meas. Tech., 8*, 4947-4977, 2015.

866 Sanghavi, S., Martonchik, J. V., Landgraf, J., and Platt, U.: Retrieval of optical depth
867 and vertical distribution of particulate scatterers in the atmosphere using O2 A-
868 and B-band SCIAMACHY observations over Kanpur: a case study, *Atmos.*
869 *Meas. Tech., 5*, 1099-1119, 2012.
870 Sasano, Y.: Tropospheric aerosol extinction coefficient profiles derived from scanning
871 lidar measurements over Tsukuba, Japan, from 1990 to 1993, *App. Opt., 35*(24),
872 4941-4952, 1996.
873 Seo, S., Kim, J., Lee, H., Jeong, U., Kim, W., Holben, B. N., Kim, S., Song, C. H., and
874 Lim, J. H.: Estimation of PM_{10} concentrations over Seoul using multiple
875 empirical models with AERONET and MODIS data collected during the
876 DRAGON-Asia campaign, *Atmos. Chem. Phys., 154*, 1-16, doi:10.5194/acp-15-
877 1-2015, 2015.
878 Shimizu, A., Sugimoto, N., Matsui, I., Arao, K., Uno, I., Murayama, T., Kagawa, N.,
879 Aoki, K., Uchiyama, A., and Yamazaki, A.: Continuous observation of Asian
880 dust and other aerosols by polarization lidars in China and Japan during ACE-
881 Asia, *J. Geophys. Res., 109*, D19S17, doi:10.1029/2002JD003253, 2004.
882 Sneep, M., De Haan, J. F., Stammes, P., Wang, P., Vanbauce, C., Joiner, J., Vasilkov, A.
883 P., and Levelt, P. F.: Three-way comparison between OMI and PARASOL
884 cloud pressure products, *J. Geophys. Res., 113*, D15S23,
885 doi:10.1029/2007JD008694, 2008.
886 Spurr, R. J. D., Kurosu, T. P., and Chance, K. V.: A linearized discrete ordinate
887 radiative transfer model for atmospheric remote-sensing retrieval, *J. Quant.*
888 *Spectro. Rad. Trans., 68*, 689-735, 2001.
889 Spurr, R. J. D.: Simultaneous derivation of intensities and weighting functions in a
890 general pseudo-spherical discrete ordinate radiative transfer treatment, *J. Quant.*
891 *Spectro. Rad. Trans., 75*, 129-175, 2002.
892 Spurr, R. J. D.: VLIDORT: A linearized pseudo-spherical vector discrete ordinate
893 radiative transfer code for forward model and retrieval studies in multilayer
894 multiple scattering media, *J. Quant. Spectro. Rad. Trans.*, *102*, 316-342, 2006.
895 Spurr, R., and Christi, M.: On the generation of atmospheric property Jacobians from
896 the (V)LIDORT linearized radiative transfer models, *J. Quant. Spectro. Rad.*
897 *Trans., 142*, 109-115, 2014.

898 Stutz, J., and Platt, U.: Numerical analysis and estimation of the statistical error of
899 differential optical absorption spectroscopy measurements with least-squares
900 methods, *Applied Optics, 35, 30*, 6041-6053, 1996.
901 Torres, O., Bhartia, P. K., Herman, J. R., Ahmad, Z., and Gleason, J.: Derivation of
902 aerosol properties from satellite measurements of backscattered ultraviolet
903 radiation: Theoretical basis, *J. Geophys. Res., 103*(14), 17099-17110, 1998.
904 Torres, O., Decae, R., Veefkind, P., and de Leeuw, G.: *OMI Aerosol Retrieval*
905 *Algorithm*, OMI Algorithm Theoretical Basis Document, Vol. III, Clouds,
906 Aerosols and Surface UV Irradiance, NASA-KNMI ATBD-OMI-03, pp. 47-71,
907 2002.
908 Torres, O., Bhartia, P. K., Sinyuk, A., Welton, E. J., and Holben, B. N.: Total Ozone
909 Mapping Spectrometer measurements of aerosol absorption from space:
910 Comparison to SAFARI 2000 ground-based observations, *J. Geophys. Res., 110,*
911 D10S18, doi:10.1029/2004JD004611, 2005.
912 Torres, O., Tanskanen, A., Veihelmann, B., Ahn, C., Braak, R., Bhartia, P. K., Veefkind,
913 P., and Levelt, P.: Aerosols and surface UV products from Ozone Monitoring
914 Instrument observations: An overview, *J. Geophys. Res., 112*, D24S47,
915 doi:10.1029/2007JD008809, 2007.
916 Twomey, S. A., Piepgrass, M., and Wolfe, T. L.: An assessment of the impact of
917 pollution on the global albedo, *Tellus, 36B*, 356-366, 1984.
918 United States Committee on Extension to the Standard Atmosphere: *US Standard*
919 *Atmosphere 1976, National Oceanic and Atmospheric Administration*, NASA.,
920 United States Air Force, Washington DC, USA, 1976.
921 Van Roozendael, M., and Fayt, C.: *WinDOAS 2.1 Software user manual*, Uccle,
922 IASB/BIRA, 2001.
923 Vandaele, A. C., Hermans, C., Simon, P. C., Carleer, M., Colin, R., Fally, S., Merienne,
924 M. F., Jenouvrier, A., and Coquart, B.: Measurements of the NO2 absorption
925 cross-section from 42000 cm^{-1} to 10000 cm^{-1} (238-1000 nm) at 220 K and 294 K, *J.*
926 *Quant. Spectrosc. Radiat. Transfer*, 59, 3-5, 171-184, 1998.
927 Veefkind, J. P., de Leeuw, G., Durkee, P. A., Russell, P. B., Hobbs, P. V., and
928 Livingston, J. M.: Aerosol optical depth retrieval using ATSR-2 and AVHRR data
929 during TARFOX, *J. Geophys. Res., 104(D2)*, 2253-2260, 1999.

930 Veihelmann, B., Levelt, P. F., Stammes, P., and Veefkind, J. P.: Simulation study of the
931 aerosol information content in OMI spectral reflectance measurements, *Atmos.*
932 *Chem. Phys.*, 7, 3115-3127, 2007.
933 Wagner, T., Dix, B., Friedeburg, C. V., Friess, U., Sanghavi, S., Sinreich, R., and Platt,
934 U.: MAX-DOAS O_4 measurements: A new technique to derive information on
935 atmospheric aerosols- Principles and information content, *J. Geophys. Res., 109*,
936 D22205, doi:10.1029/2004JD004904, 2004.
937 Wagner, T., Beirle, S., Deutschmann, T., Grzegorski, M., and Platt, U.: Satellite
938 monitoring of different vegetation types by differential optical absorption
939 spectroscopy (DOAS) in the red spectral range*, Atmos. Chem. Phys., 7*, 69-79,
940 2007.
941 Wagner, T., Deutschmann, T., and Platt, U.: Determination of aerosol properties from
942 MAX-DOAS observations of the Ring effect, *Atmos. Meas. Tech., 2*, 495-512,
943 2009.
944 Wagner, T., Beirle, S., Deutschmann, T., and de Vries, M. P.: A sensitivity analysis of
945 Ring effect to aerosol properties and comparison to satellite observations, *Atmos.*
946 *Meas. Tech., 3*, 1723-1751, 2010.
947 Wang, J., and Christopher, S. A.: Intercomparison between satellite-derived aerosol
948 optical thickness and PM2.5 mass: Implications for air quality studies, *Geophys.*
949 *Res. Lett.,30*(21), 2095, doi:10.1029/2003GL018174, 2003.
950 Wang, P., Tuinder, O. N. E., Tilstra, L. G., and Stammes, P.: Interpretation of FRESCO
951 cloud retrievals in case of absorbing aerosol events, *Atmos. Chem. Phys., 12*,
952 9057-9077, 2012.
953 Watson, J. G., Chow, J. C., Lu, Z., Fujita, E. M., Lowenthal, D. H., Lawson, D. R., and
954 Ashbaugh, L. L.: Chemical mass balance source apportionment of PM10 during
955 the Southern California air quality study, *Aerosol Sci. Technol., 21(1)*, 1-36,
956 1994.
957 Yang, K., Liu, X., Bhartia, P. K., Krotkov, N. A., Carn, S. A., Hughes, E. J., Krueger, A.
958 J., Spurr, R. J. D., and Trahan, S. G.: Direct retrieval of sulfur dioxide amount
959 and altitude from spaceborne hyperspectral UV measurements: Theory and
960 application, *J. Geophys. Res., 115*, D00L09, doi:10.1029/2010JD013982, 2010.

961 Zhang, H., Lyapustin, A., Wang, Y., Kondragunta, S., Laszlo, L., Ciren, P., and Hoff, R.
962 M.: A multi-angle aerosol optical depth retrieval algorithm for geostationary
963 satellite data over the United States, *Atmos. Chem. Phys., 11*, 11977-11991,
964 2011.
965
966

967 **List of Tables**

976

977 **List of Figures**

1005

Tables

Table 1. The database of cross section used for DOAS fitting analysis.

Species	Temperature (K)	Reference
O_3	223, 243, and 273	Bogumil *et al.* (2001)
NO_2	220 and 294	Vandaele *et al.* (1998)
O_4	298	Hermans *et al.* (1999)

Table 2. Dimensions of LUT for the clear sky comparison.

Variable name	No. of Entries	Entries
SZA	7	0, 10, 20, 30, 40, 50, 60 degrees
VZA	7	0, 10, 20, 30, 40, 50, 60 degrees
RAA	10	0, 20, 40, 60, 80, 100, 120, 140, 160, 180 degrees

SZA : Solar zenith angle, VZA : Viewing zenith angle, RAA: Relative azimuth angle.

Table 3. Dimensions of simulation cases for the error analysis of the AEH retrieval.

Variable name	No. of Entries	Entries
SZA	7	0, 10, 20, 30, 40, 50, 60 degrees
VZA	7	0, 10, 20, 30, 40, 50, 60 degrees
RAA	10	0, 20, 40, 60, 80, 100, 120, 140, 160, 180 degrees
AOD	5	0.4, 1.0, 1.6, 2.5, 3.0
AEH	8	1.0, 1.2, 1.6, 2.0, 2.4, 3.0, 4.0, 5.0 km
Aerosol Model	3	MITR, WASO, COPO
Surface Albedo	1	0.10

Table 4. Absolute difference of O4I for changing surface albedo by 0.02.

	MITR	WASO	COPO
Maximum	81	85	76
Case [AOD,AEH]	[0.4,5.0]	[0.4,5.0]	[0.4,5.0]
Minimum	8	11	1
Case [AOD,AEH]	[3.0,1.0]	[3.0,1.0]	[3.0,1.0]
Mean	38±22	37±20	20±21

Table 5. The error for AEH due to the change in aerosol vertical distribution.

Reference shape (Exponential)	MITR (Gaussian)	WASO (Gaussian)	COPO (Gaussian)
Error for AEH [m]	1477±602	671±265	722±190

Table 6. Summary of error sources and total error budget for the AEH retrieval.

Error source	MITR	WASO	COPO
AOD (ΔAOD = 0.2)	387±740 m	105±131 m	218±358 m
SSA (10% change)	726±537 m	1047±194 m*	576±332 m
Surface Albedo ($\Delta\alpha$ = 0.02)	438±762 m	199±241 m	154±274 m
Particle Size (20% change)	352±174 m	72±56 m	315±213 m
Atmospheric Gases		< 5 m	
Atmospheric Pressure** (ΔP = 3%)		3.4±0.1% (O_4 SCD)	
Instrument (Shift : 0.02 nm)		<10 m	
Total Error	1276 m	846 m	739 m

* Calculation results for the SSA decrease by 10%.

** For clear sky calculation.

1027 Table 7. Dimensions of LUT for the AEH algorithm using OMI.

Variable name	No. of Entries	Entries
SZA	7	0, 10, 20, 30, 40, 50, 60 degrees
VZA	7	0, 10, 20, 30, 40, 50, 60 degrees
RAA	10	0, 20, 40, 60, 80, 100, 120, 140, 160, 180 degrees
AOD	13	0.0, 0.2, 0.4, 0.6, 0.8, 1.0, 1.3, 1.6, 1.9, 2.2, 2.5, 3.0, 5.0
AEH	16	0.0, 1.0, 1.2, 1.4, 1.6, 1.8, 2.0, 2.2, 2.4, 2.6, 2.8, 3.0, 3.5, 4.0, 5.0, 10.0 km
Aerosol Model	3	Dust, Carbonaceous, Non-absorbing [Climatology over East Asia site of AERONET]

1028

1029 Table 8. List of aerosol transport cases and its period for comparison.

Case	Period
1	March, 28, 2007 - April, 2, 2007
2	May, 5, 2007 - May, 10, 2007
3	May, 25, 2007 - May, 26, 2007
4	February, 19, 2008 - February, 21, 2008
5	April, 3, 2008 - April, 5, 2008
6	May, 28, 2008 - May, 31, 2008
7	December, 4, 2008 - December, 7, 2008

1030

Figures

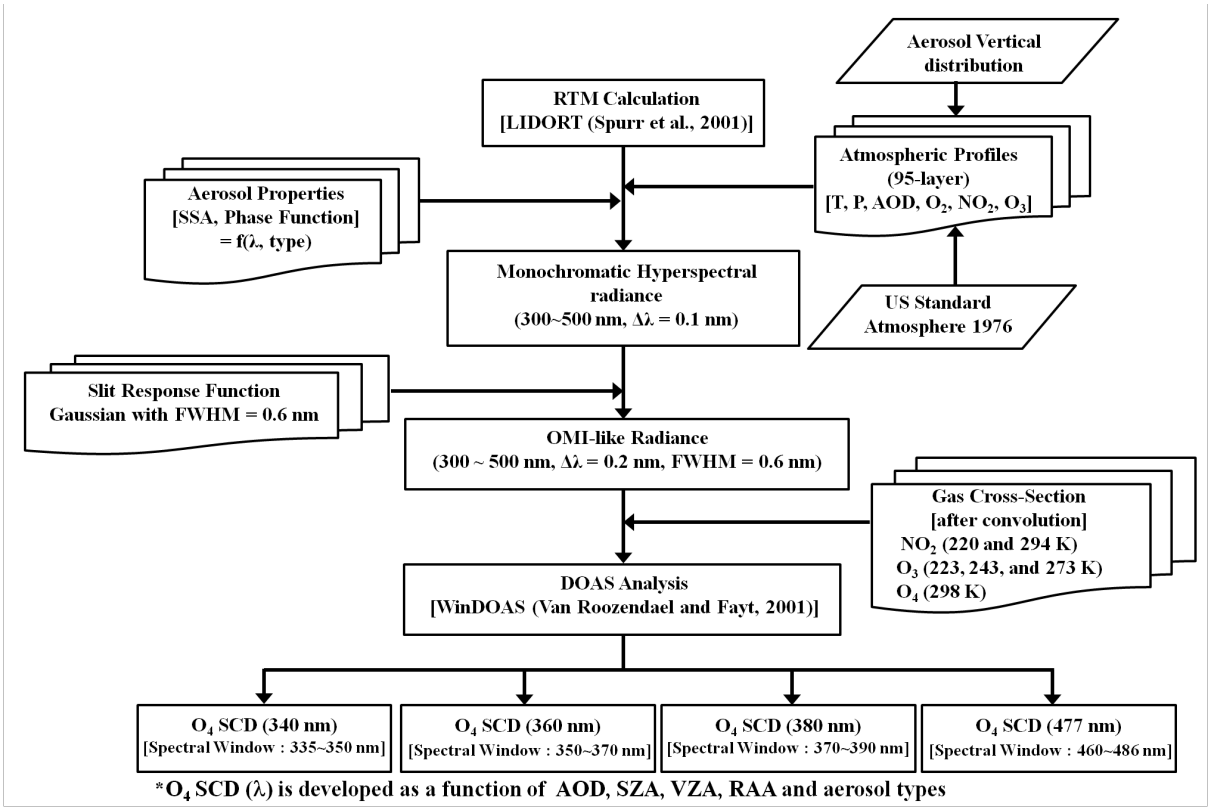

Figure 1. Flowchart of the simulated O_4 SCD estimation.

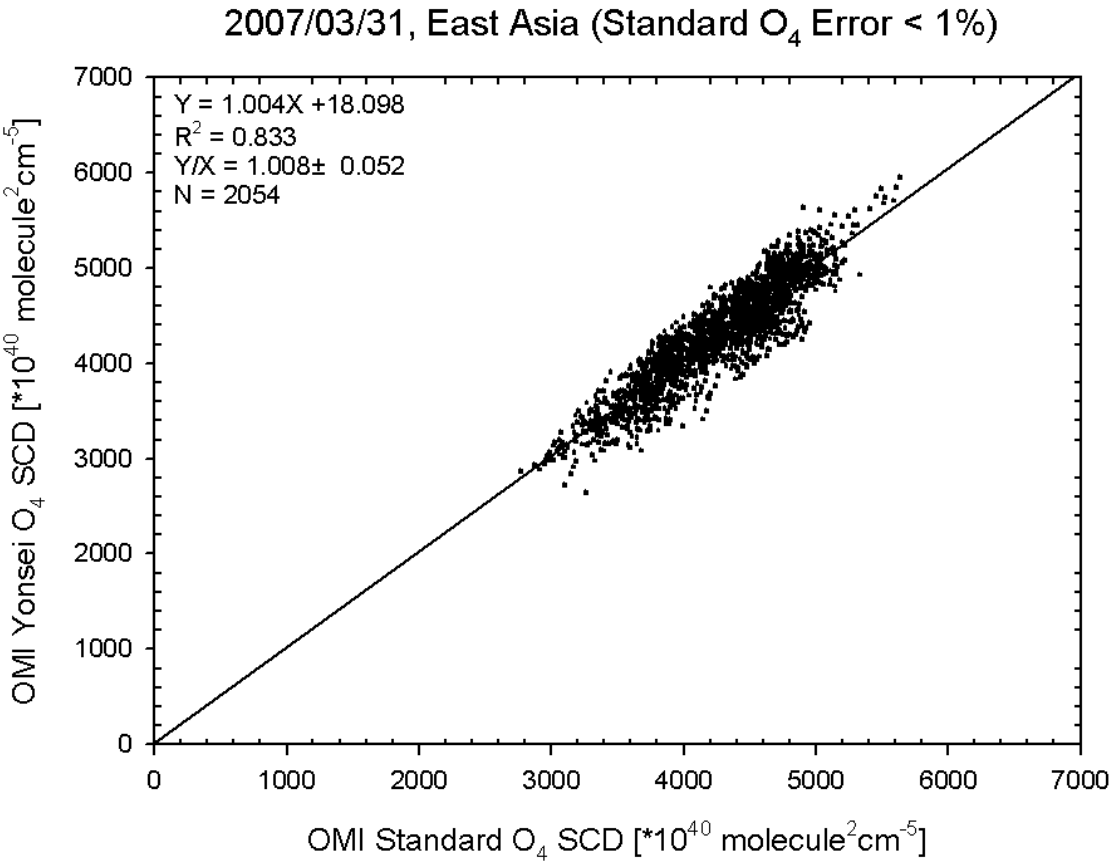

Figure 2. Comparison of O_4 SCD directly retrieved from OMI radiance with the OMI standard product on March 31, 2007.

(a)

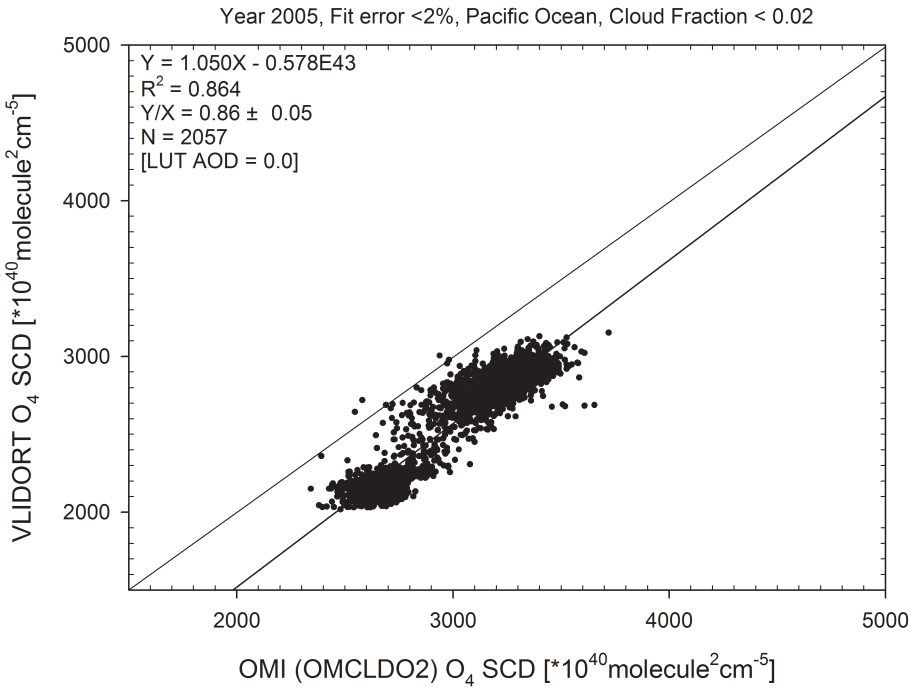

(b)

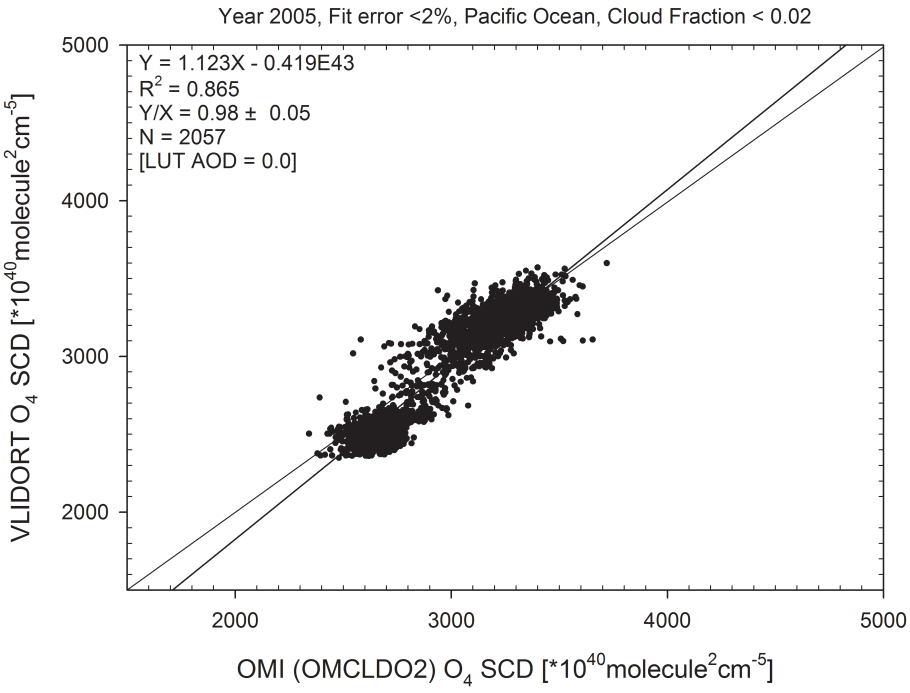

Figure 3. Comparison of the O_4 SCD at 477 nm between the OMI standard product and the calculated value from LUT (a) before and (b) after correction of LER.

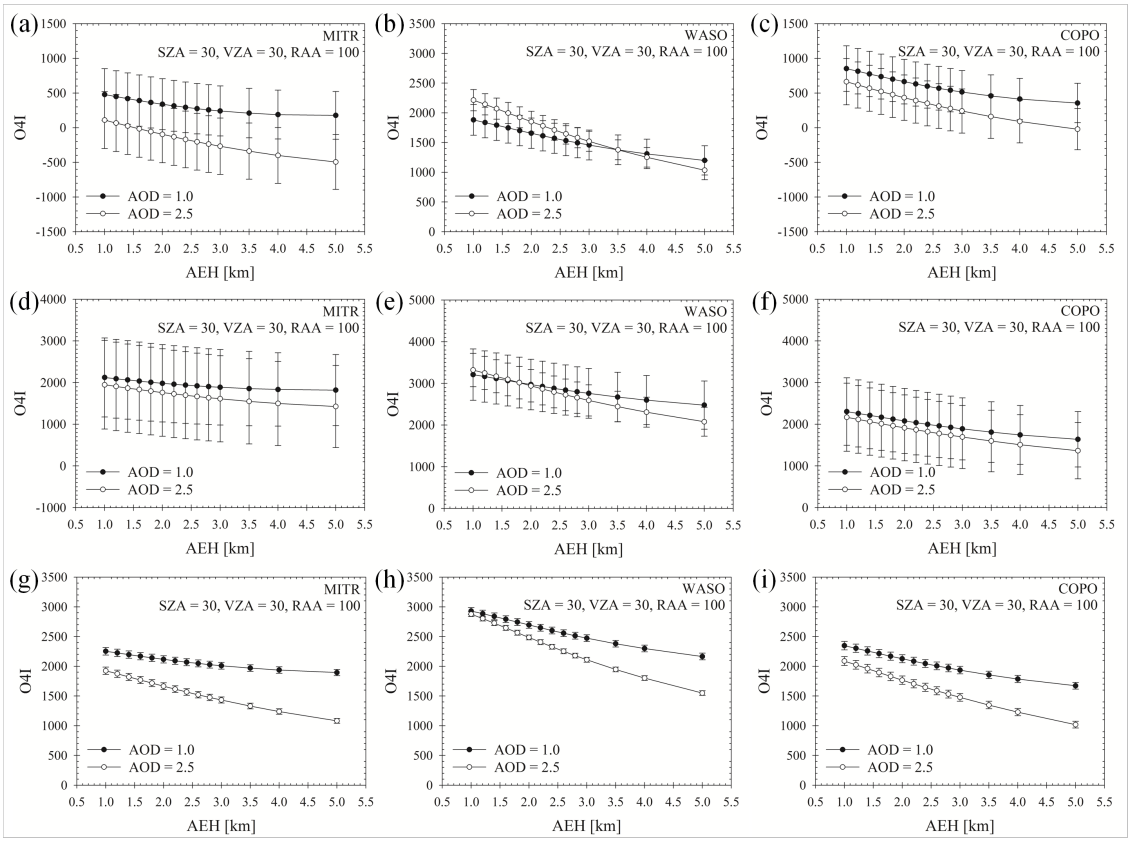

Figure 4. The O4I at 360 nm band for (a) MITR, (b) WASO, and (c) COPO, (d) at 380 nm band for MITR, (e) WASO, and (f) COPO, and (g) at 477 nm band for MITR, (h) WASO, and (i) COPO as a function of AEH.

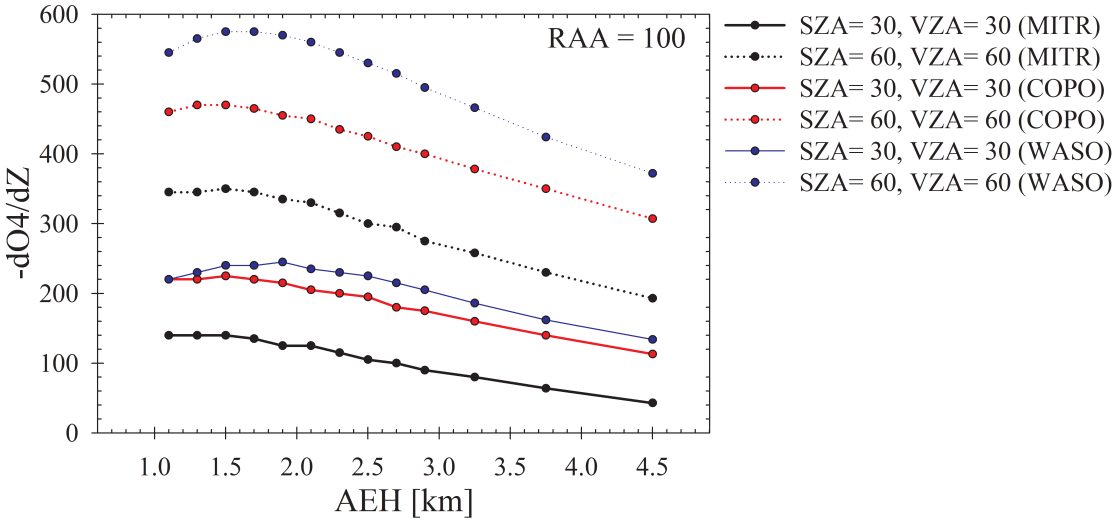

Figure 5. The AEH sensitivity to O4I (-dO4/dZ) with changing observation geometries at 477 nm.

(a)

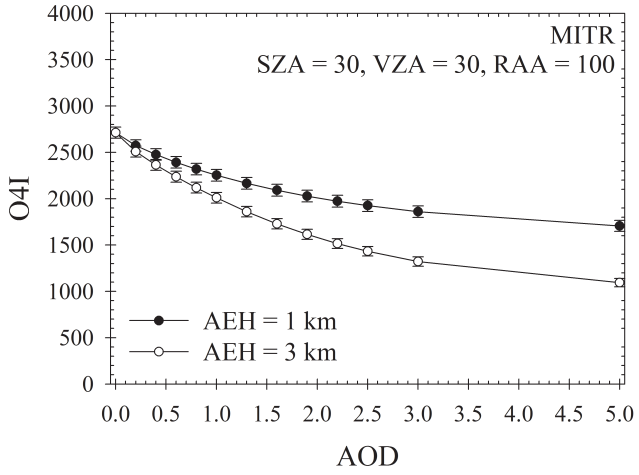

(b)

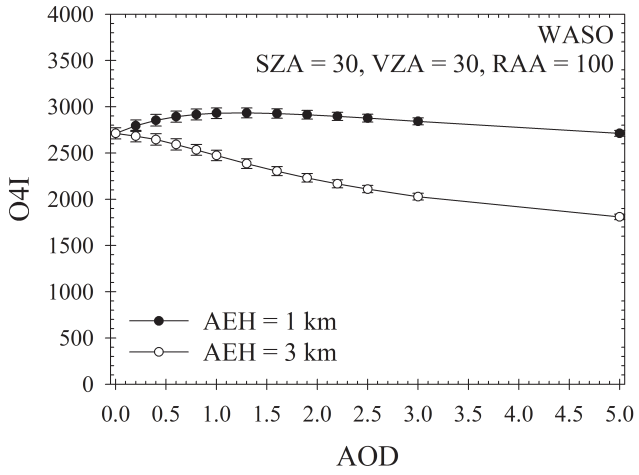

(c)

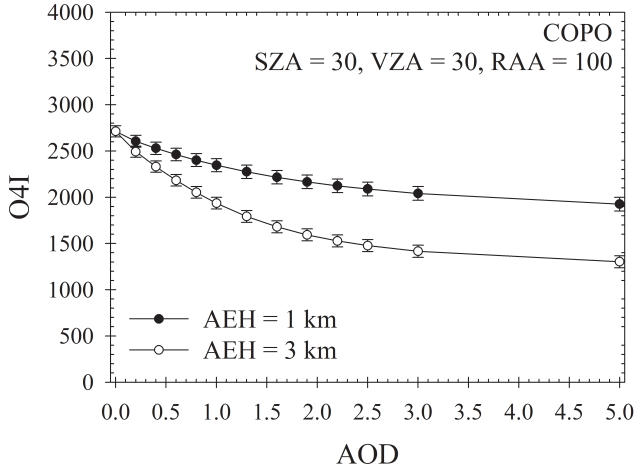

Figure 6. The O4I of (a) MITR, (b) WASO, and (c) COPO types as a function of AOD.

(a)

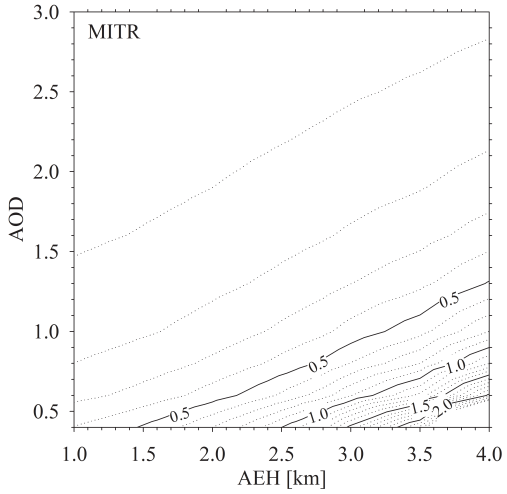

(b)

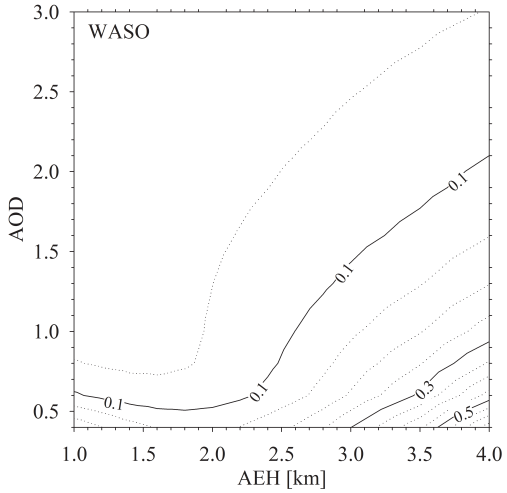

(c)

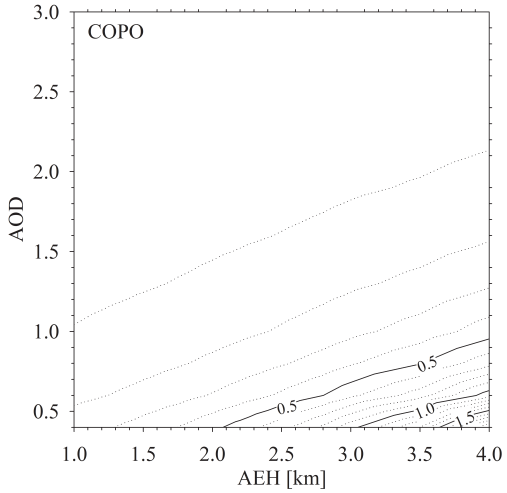

Figure 7. AEH error of (a) MITR, (b) WASO, and (c) COPO for the AOD difference of 0.1 as a function of reference AEH and AOD.

(a)

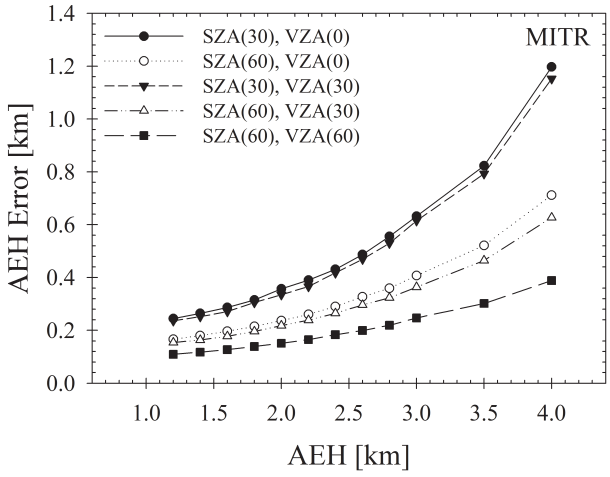

(b)

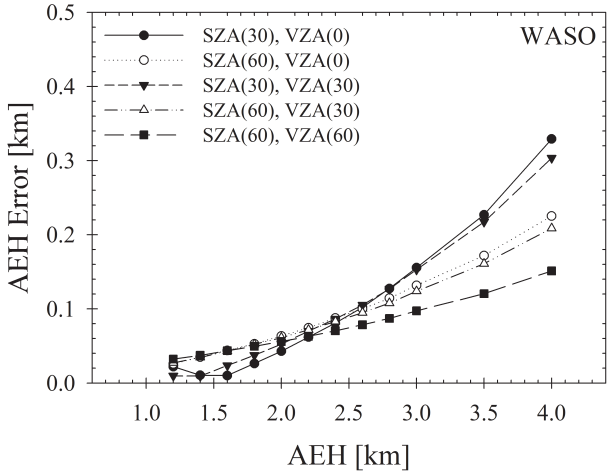

(c)

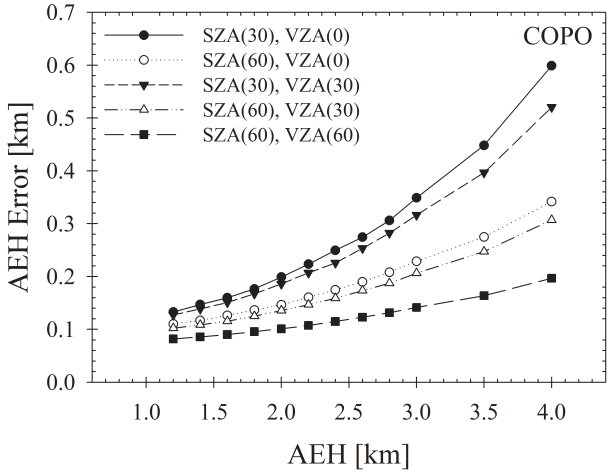

Figure 8. AEH error of (a) MITR, (b) WASO, and (c) COPO for the AOD difference of 0.1 as changing viewing geometries.

(a)

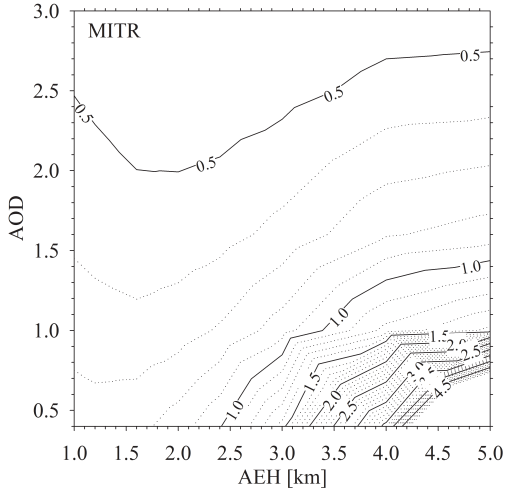

(b)

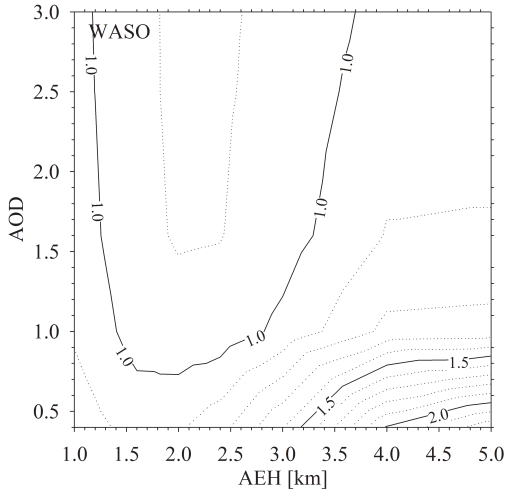

(c)

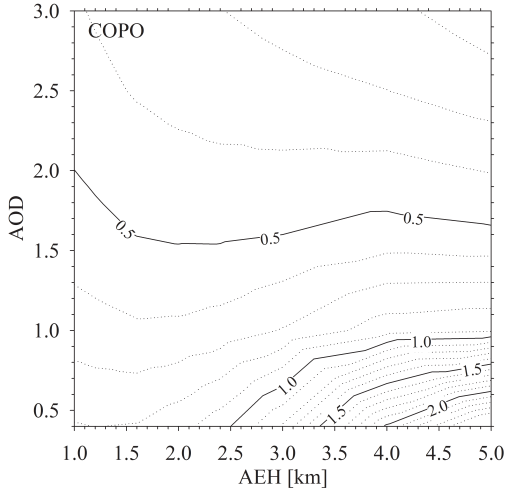

Figure 9. Same as Figure 7 except for SSA difference of 10%.

(a)

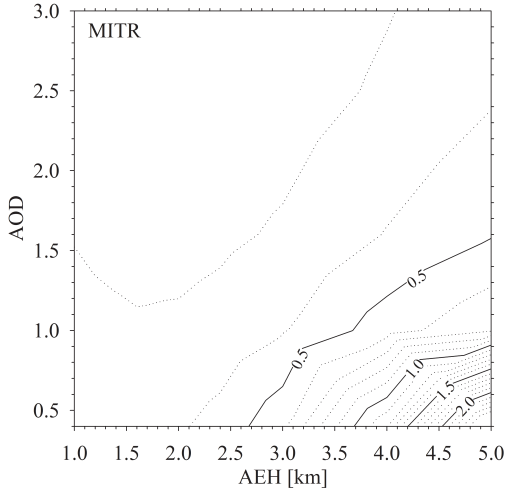

(b)

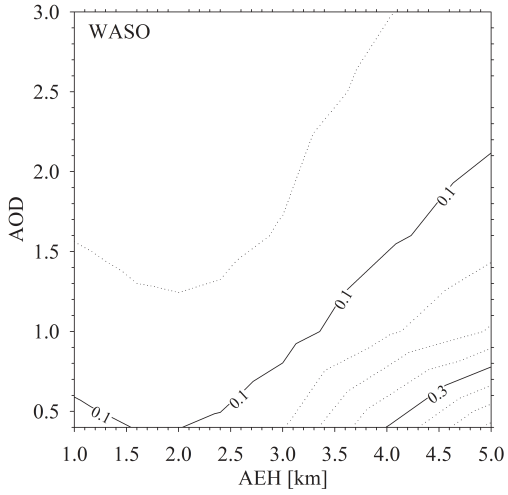

(c)

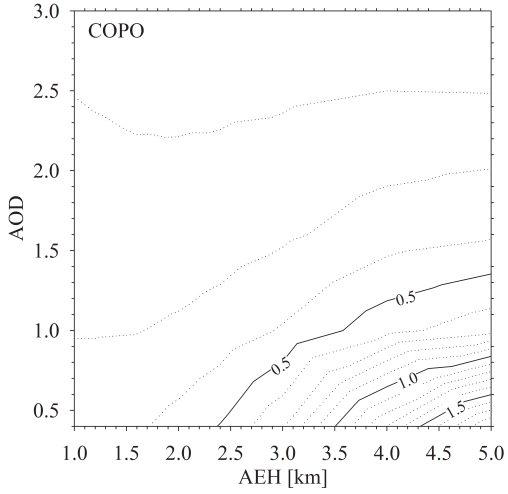

Figure 10. Same as Figure 7 except for particle size difference of 20%.

(a)

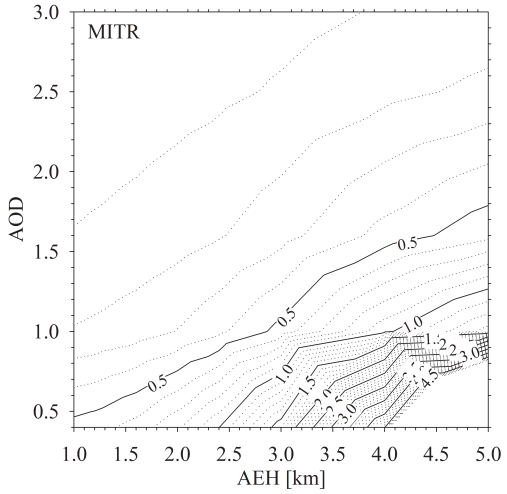

(b)

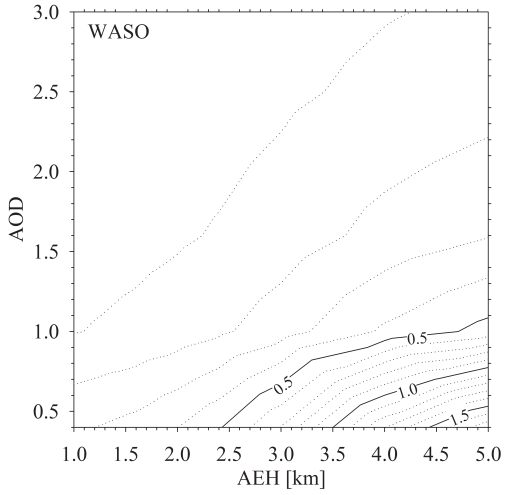

(c)

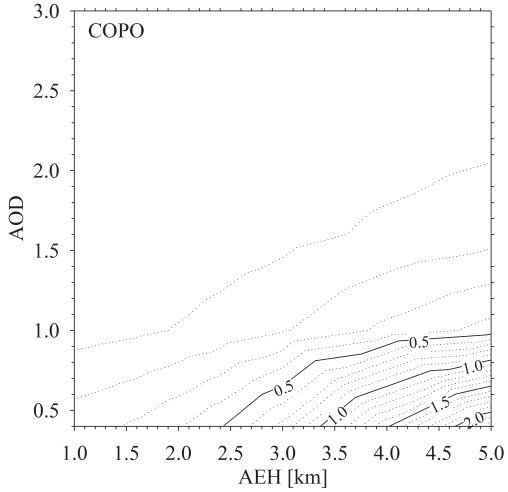

Figure 11. Same as Figure 7 except for surface albedo difference of 0.02.

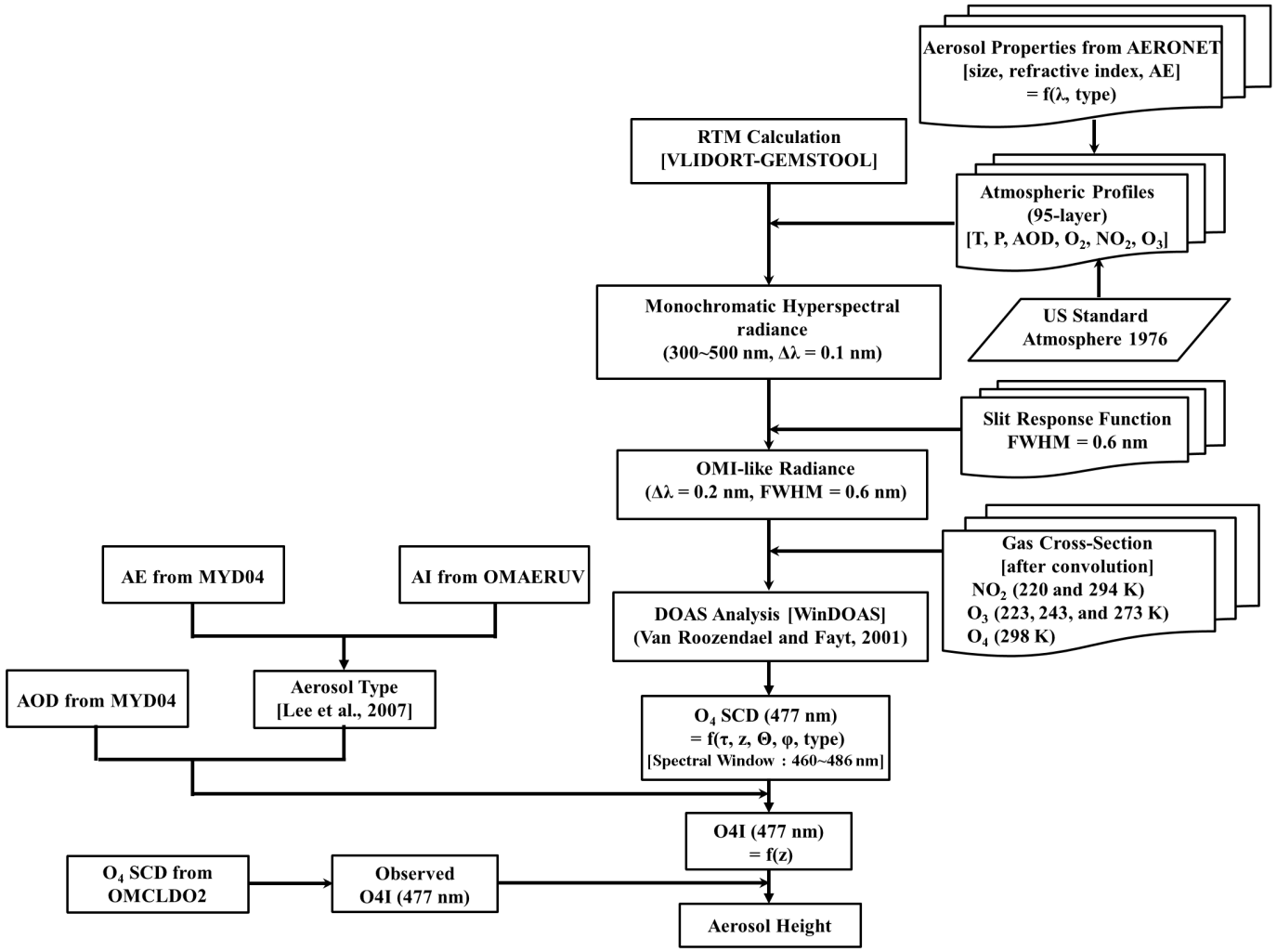

Figure 12. Flowchart of the retrieval algorithm for AEH from OMI observation.

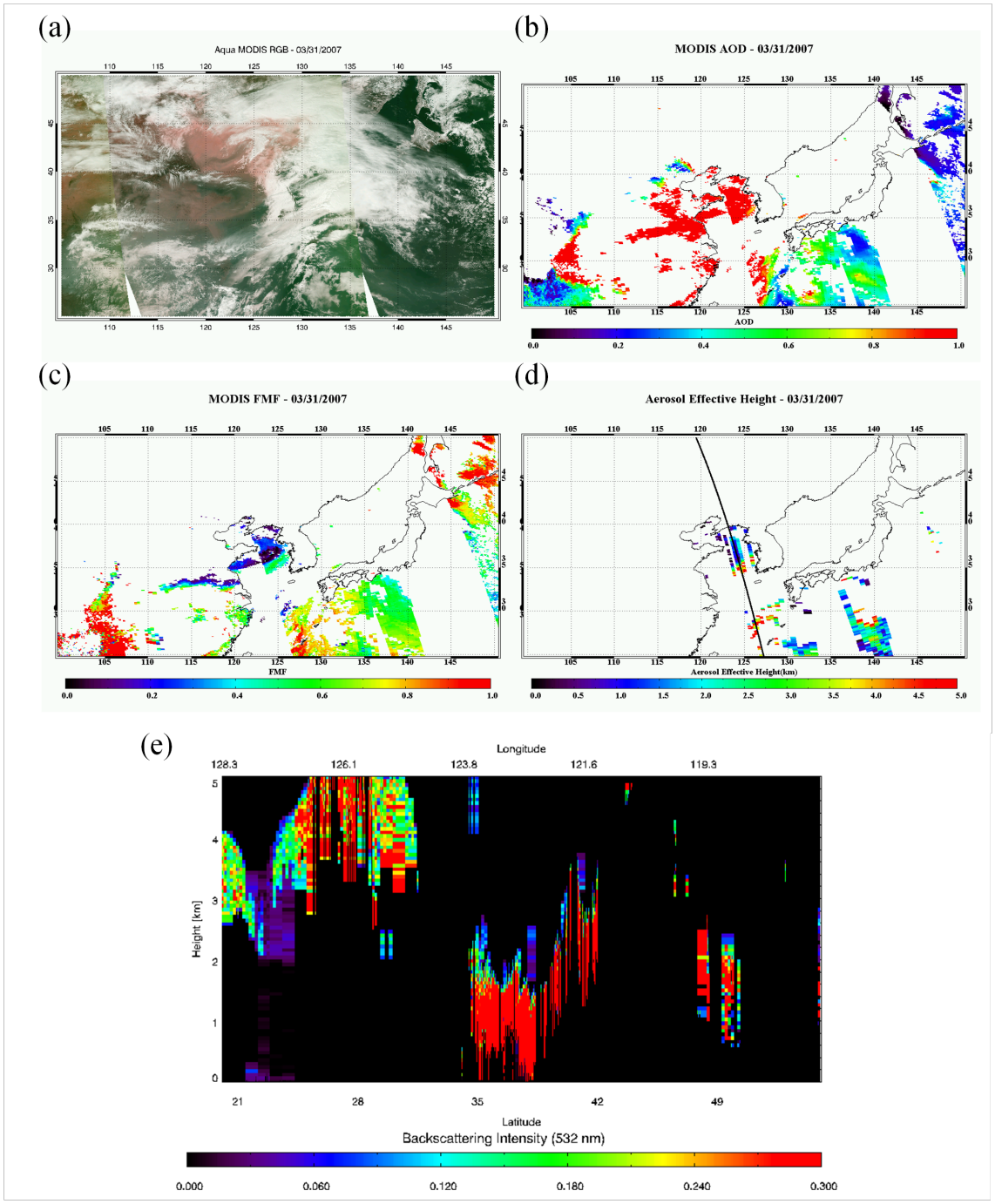

Figure 13. (a) MODIS RGB, (b) AOD, (c) FMF, and (d) AEH distribution from OMI over East Asia, and (e) backscattering Intensity at 532 nm from CALIOP observation over Yellow Sea on March 31, 2007.

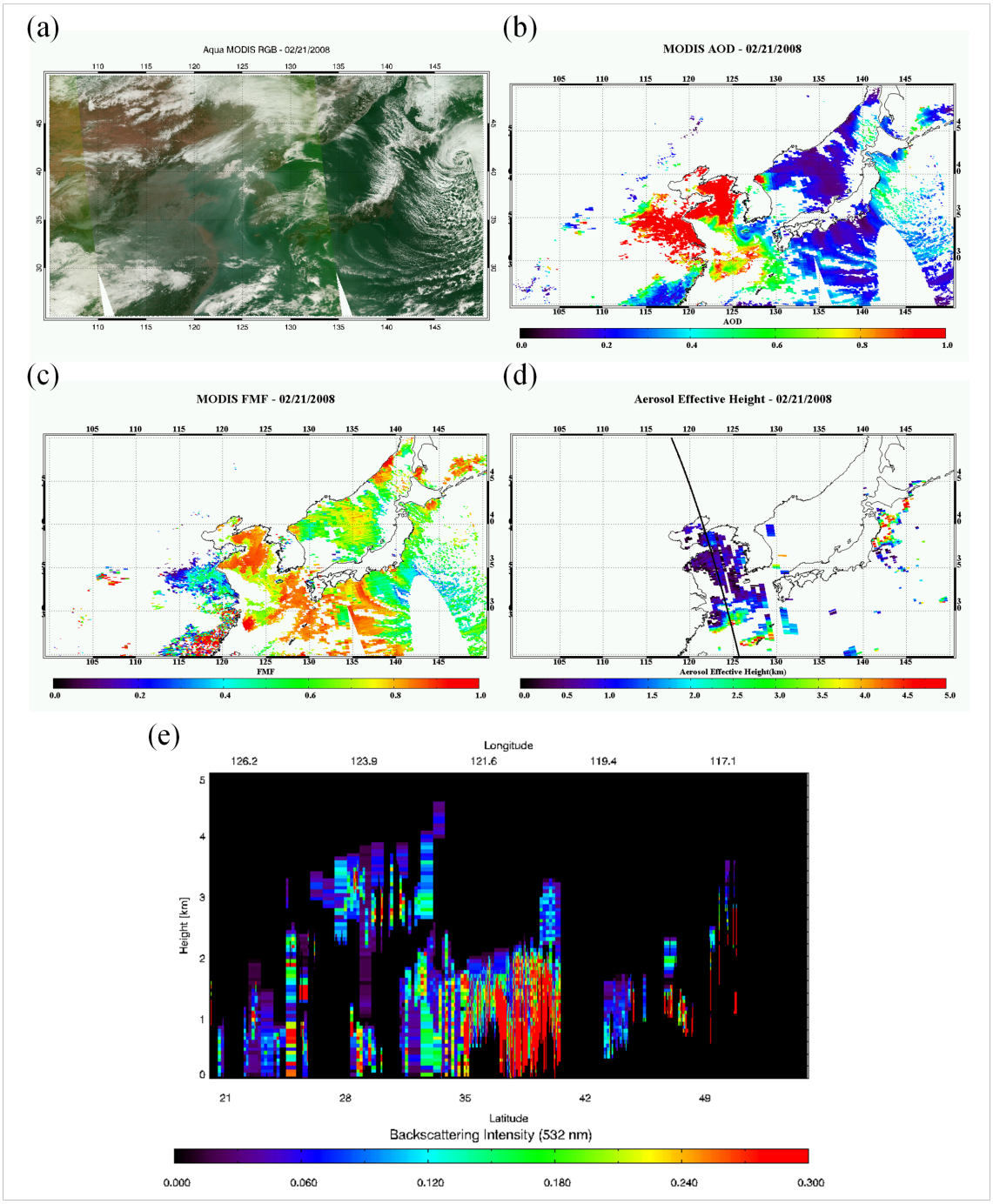

Figure 14. (a) MODIS RGB, (b) AOD, (c) FMF, and (d) AEH distribution from OMI over East Asia, and (e) backscattering Intensity at 532 nm from CALIOP observation over coastal region of China on February 21, 2008.

(a)

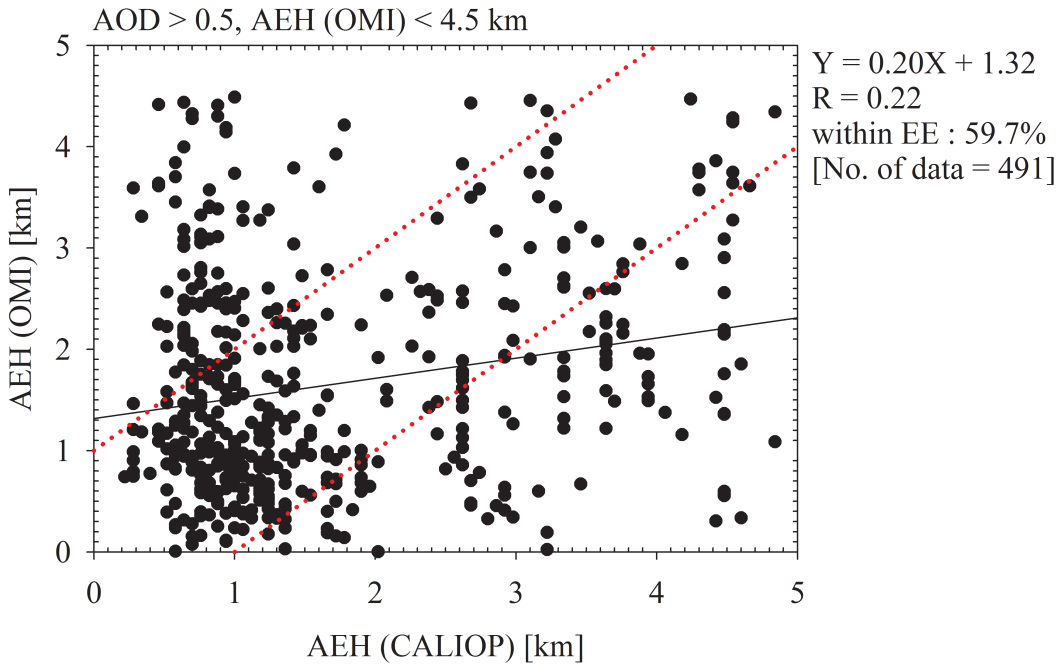

(b)

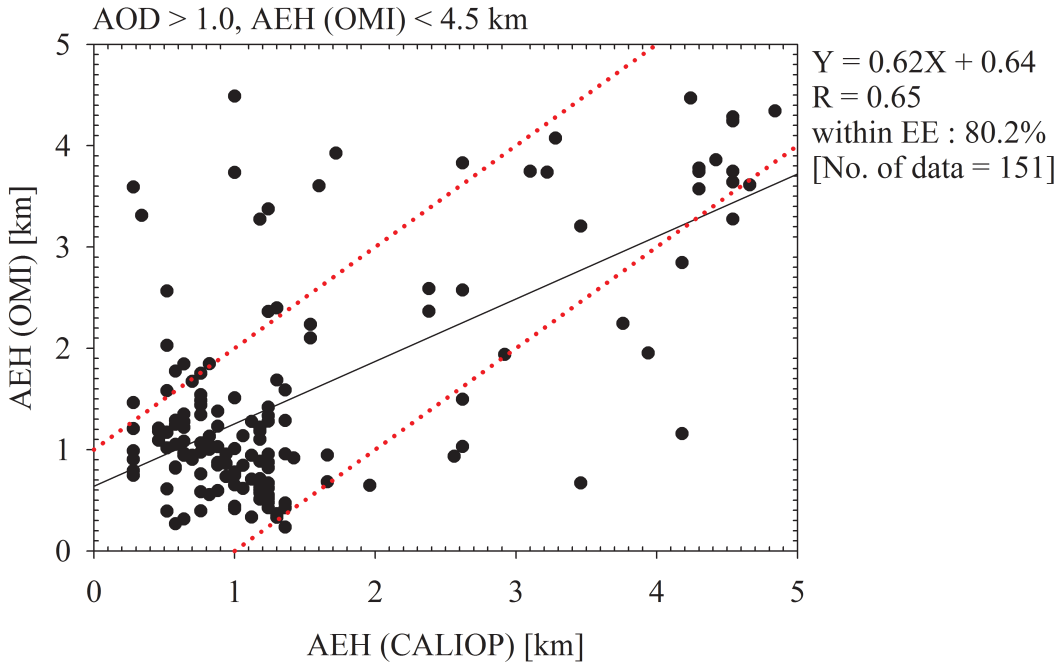

Figure 15. Comparison of AEH from OMI with CALIOP with (a) AOD > 0.5, and (b) AOD > 1.0 for aerosol transport cases in 2007 and 2008 over East Asia.